



## Optimum parameters for each subject in bone remodeling models: A new methodology using surrogate and clinical data<sup>☆</sup>

Gabriela Wessling Oening Dicati <sup>a,b,\*</sup>, José Eduardo Gubaua <sup>a,b</sup>, Jucélio Tomás Pereira <sup>a,b,c</sup>

<sup>a</sup> Postgraduate Program in Mechanical Engineering (PG-Mec), Federal University of Paraná (UFPR), Polytechnic Center, Curitiba, Brazil

<sup>b</sup> Laboratory of Computational Solid Mechanics (LaSCom), Federal University of Paraná (UFPR), Curitiba, Brazil

<sup>c</sup> Mechanical Engineering Department, Federal University of Paraná (UFPR), Polytechnic Center, Curitiba, Brazil

### ARTICLE INFO

#### Keywords:

Numerical uniqueness of solution  
Finite element method  
Kriging  
Computerized tomography  
Individualization of bone remodeling model

### ABSTRACT

Bone remodeling models use experimental and theoretical parameters to simulate bone tissue behavior. The physical parameters are computed satisfactorily using numerical methods, e.g., the density distribution. Different subjects require specific parameters. However, traditional bone remodeling models do not consider distinct parameters for each subject. We aim to present a new methodology that accounts for specific parameters for each subject while reviewing bone remodeling, biological aspects, and coupling with the finite element method. We divide the new methodology into three steps: (a) obtaining the density distribution from the femur tomography and a finite element model; (b) implementing an algorithm for bone remodeling via Abaqus; and (c) implementing a Matlab code that combines the design of experiments, surrogate, bone remodeling model, and the finite element method to minimize the difference between the clinical and numerical density distributions. Furthermore, we considered subjects' characteristics as the physical activity amount and body mass in the numerical simulations. The new methodology is valid whenever the remodeling model presents a tendency towards solution uniqueness. We applied the new methodology in 18 subjects and obtained a different set of parameters for each one. These parameters allowed characterizing a more accurate and realistic femoral density distribution for each subject. Furthermore, the new methodology decreased the density relative difference by 50%, compared with the traditional ones.

### 1. Introduction

The bone tissue is a live, porous, and anisotropic material. It is under constant modification due to external and internal stimuli, e.g., day-to-day activities and hormones. The bone is a heterogeneous structure composed by organic and mineral phased that provide tensile strength and rigidity in both traction and compression (Cowin, 2001; Doblaré and García, 2002; Komarova et al., 2003; Doblaré et al., 2004; Lemaire et al., 2004; Rüberg et al., 2005; Belinha et al., 2013). The bone tissue has a natural process called bone remodeling (BR), responsible for replacing old and damaged tissue and allowing the bone tissue to adapt to different load configurations (Komarova et al., 2003; Lemaire et al., 2004; Pivonka et al., 2008). The BR is also associated with microdamage repair, which is formed due to fatigue and overload, and the maintenance of mineral salts in the human body, mainly calcium (Hazelwood et al., 2001; Doblaré and García, 2002; Komarova et al., 2003; Rüberg et al., 2005; Scheiner et al., 2013; Klika et al.,

2014). The organized activities of two phenotypes of bone cells, called osteoblasts and osteoclasts, perform the tissue renewal and are responsible for bone formation and resorption, respectively. Inside a cellular structure known as the Basic Multicellular Unit (BMU), the cells perform organized activities following the A-R-F sequence (Activation–Resorption–Formation) (Frost, 1987; Cowin, 2001; Rüberg et al., 2005; Cooper et al., 2006; Hadjifakis and Androulakis, 2006; Pivonka et al., 2008; Ryser et al., 2009; Cardoso et al., 2013; Burr and Allen, 2014; Klika et al., 2014; Oumghar et al., 2020). A third cell phenotype is the osteocytes, which are osteoblasts embedded in the bone matrix after the complete formation of new bone tissue. They are responsible for mechanosensing and mechanotransduction of the mechanical and biochemical stimuli (Komarova et al., 2003; Doblaré et al., 2004; Lemaire et al., 2004; Scheiner et al., 2013; Burr and Allen, 2014; Della Corte et al., 2020). Essentially, the osteocytes have the capability “to feel” the external load and transform it into biochemical signals, starting

<sup>☆</sup> This study was financed in part by the Coordenação de Aperfeiçoamento de Pessoal de Nível Superior - Brasil (CAPES) - Finance Code 001.

\* Correspondence to: Universidade Federal do Paraná - Centro Politécnico, Av. Cel. Francisco H. dos Santos, 100 - Jardim das Américas, Curitiba - PR, 81530-000, Bloco IV, sala PG-18

E-mail addresses: [gabioening@gmail.com](mailto:gabioening@gmail.com) (G.W.O. Dicati), [gubaua@ufpr.br](mailto:gubaua@ufpr.br) (J.E. Gubaua), [jucelio.tomas@ufpr.br](mailto:jucelio.tomas@ufpr.br) (J.T. Pereira).

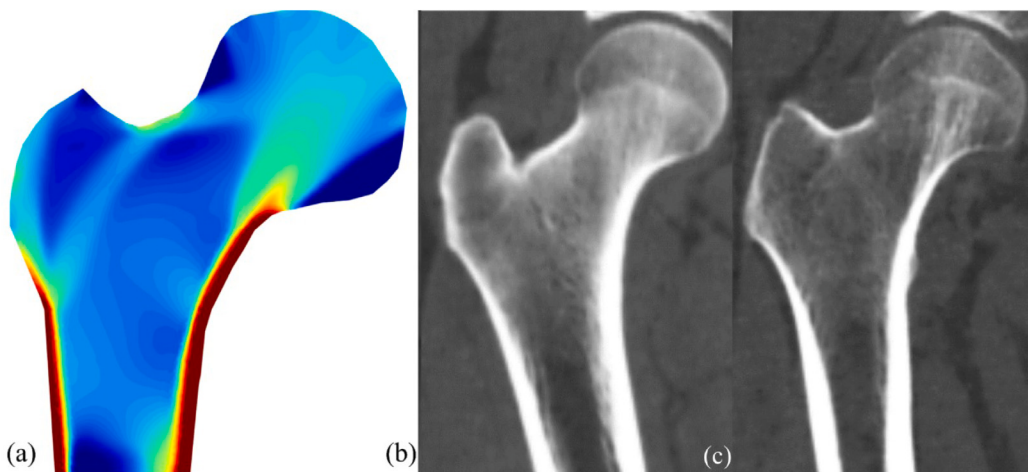


**Fig. 1.** Density distributions of the human femur and its particularities. (a) Numerical density distribution, and data from CT scan of (b) 31-year-old and (c) 62-year-old subjects.

the BR process (Bonewald, 2006, 2007; You et al., 2008; Schaffler and Kennedy, 2012; Cardoso et al., 2013; Burr and Allen, 2014; Hinton et al., 2018; Oumghar et al., 2020). Such mechanical stimuli are associated with, for instance, accumulated microdamage that disrupts the osteocytes network (Schaffler and Kennedy, 2012; Burr and Allen, 2014), the mechanical strains around the osteocytes (Frost, 1987; Oz-civici et al., 2010; Bonewald, 2011), the fluid shear stress acting on the cell membrane and processes (Reich et al., 1990; Jacobs et al., 2010; Rieger et al., 2011), and the lacunar pore hydrostatic pressure (Scheiner et al., 2016).

In the literature, one can find several models that aim to simulate the BR process through different approaches, e.g., phenomenological, biological, and mechanobiological (Beaupré et al., 1990; Huiskes et al., 1992; Jacobs et al., 1995; Doblaré and García, 2002; Lemaire et al., 2004; Rüberg et al., 2005; McNamara and Prendergast, 2007; Pivonka et al., 2008; Cardoso et al., 2013; Scheiner et al., 2013; Martin et al., 2019; Ashrafi et al., 2020; Bahia et al., 2020; Gubaua et al., 2020). Phenomenological models describe the bone tissue behavior by comparing the computed mechanical stimulus with the reference mechanical stimulus. Mainly, because there is no biological consideration (Beaupré et al., 1990; Weinans et al., 1992; Jacobs et al., 1995, 1997; Doblaré and García, 2002). The biological models account for the cells involved in the BR and body biochemical factors. In these models, one can numerically evaluate the cellular processes such as differentiation, activation, apoptosis, formation, and resorption of bone tissue using non-linear differential equations. (Kroll, 2000; Komarova et al., 2003; Lemaire et al., 2004; Boyce and Xing, 2008; Pivonka et al., 2008; Ryser et al., 2009; Tyrovolas and Odont, 2015). Mechanobiological models associate cellular responses with mechanical stimuli. However, the BMU behavior is phenomenologically described (Hernandez et al., 2000; Hazelwood et al., 2001; Rüberg et al., 2005; Martínez-Reina et al., 2009). Other BR models also account for chemical reactions induced by mechanical stimulus (mechanoreception) and its consequent transformation into biochemical signals. These signals are transmitted to other cells (mechanotransduction) to start the BR process (Adachi and Kameo, 2006; Scheiner et al., 2013; Avval et al., 2014; Hamblin, 2014; Klika et al., 2014; Mercuri et al., 2016; Pastrama et al., 2018; Cerrolaza et al., 2019; Martin et al., 2019; Ashrafi et al., 2020). Finally, some models simulate bone tissue behavior using pharmacokinetic-pharmacodynamic models that include the effect of drugs (Trichilo et al., 2019; Bahia et al., 2020; Ashrafi et al., 2021).

The coupling between the phenomenological models and Finite Element Method (FEM) allows the simulation of the tissue behavior regarding the applied load (see, e.g., Weinans et al. (1992), Jacobs et al. (1995, 1997), Doblaré and García (2001)). For instance, in the femur case it is possible to obtain a density distribution when loads

resulting from a gait cycle are applied. The bone density distribution, in its steady-state condition, qualitatively characterizes the bone morphology. Fig. 1a shows a density distribution obtained from a numerical simulation of the proximal part of the human femur by considering a BR model, and Fig. 1b and 1c show computerized topographies (CT) images of human femurs for two subjects of significantly different ages. One can note that there are several discrepancies between the numerical and clinical density distributions. That is, the numerical density distribution is just a qualitative representation. A density distribution achieved from the numerical simulation that is as close to the clinical as possible is difficult to obtain, since each subject has a singular density distribution (Fig. 1b and 1c). Such distribution is unique due to, e.g., age, gender, physical condition, ethnicity, food, and health condition. Besides that, the BR models parameters are generally empirically determined, and there is no ideal configuration for each subject.

It is common to find parametric analysis in BR. For example, the study presented by Beaupré et al. (1990), which determined the reference mechanical stimulus of their model from experimental data and theoretical analysis. The authors related a experimentally measured daily walk step quantity to a level of strain at the bone site and an exponent that characterizes the activity. The authors indicated three values and, after performing the simulations, they determined that the reference mechanical stimulus of 50.0 MPa would be ideal. Thomsen et al. (1994, 2020) aimed to obtain a density distribution of a vertebra similar to that found after menopause. They performed a sensibility analysis for two parameters of BR model: the activation frequency and the resorption depth. Turner et al. (2005) used the BR model proposed by Huiskes et al. (1992), and applied it to a 3D femur geometry to predict changes in the density distribution after a total hip replacement. Furthermore, the authors modified the width of the lazy zone and the rates of bone formation and resorption. Sharma et al. (2009) performed an analysis on a glenoid using the BR model proposed by Weinans et al. (1992). They changed the width of the lazy zone, rate of remodeling, and range of time in which BR occurs for each increment. In all these works, the sensibility analysis of the parameters was performed with predetermined values, which allowed a qualitative evaluation of the bone tissue behavior for different external and internal stimuli.

The results can also be evaluated quantitatively, in which one can compare the difference between the numerical density distribution and the one obtained via CT. This comparison is one of the aims proposed in by Pérez et al. (2008), where the authors simulated the BR process using the model proposed by Doblaré and García (2002), in the femur, tibia, and mandible. The authors implemented a code to calculate the absolute and relative differences. Then, they performed the comparison between the numerical and clinical distributions. Neuert and Dunning

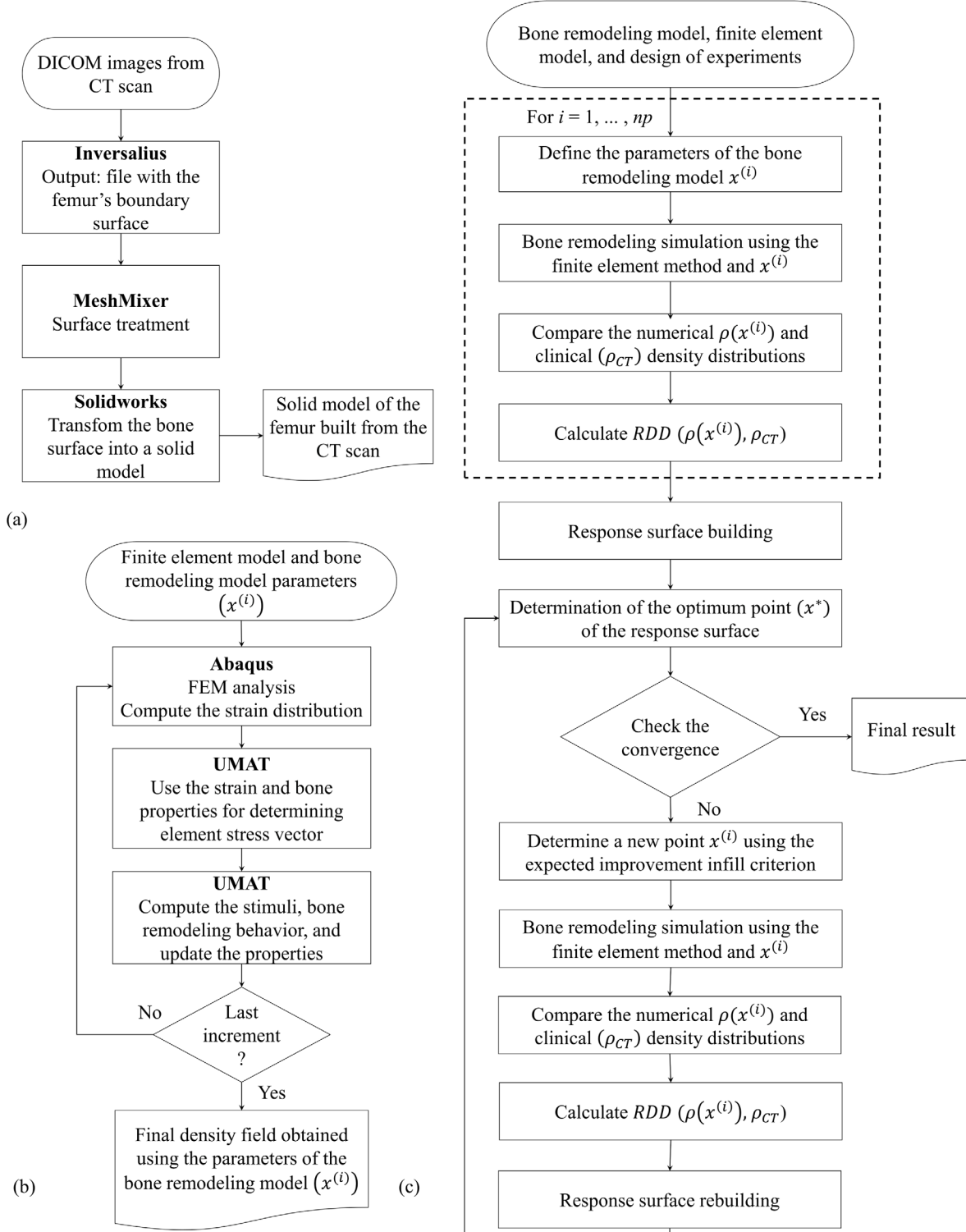


Fig. 2. Flowcharts: (a) solid model building of the human femur, (b) generic for the BR process, and (c) general structure of the new methodology.

(2013) proposed a study that coupled the solution sensitivity concerning the model parameters with a quantitative analysis. In this study, the objective was to obtain the best solution for characterizing the density distribution of the distal portion of an ulna, using the BR model proposed by Weinans et al. (1992). The authors changed the parameters regarding the width of the lazy zone and the reference mechanical stimulus. An error measure, called mean square error, was obtained and used to evaluate the quality of each configuration.

In all mentioned works, the authors previously defined the parameters variations. In studies involving a quantitative analysis, the authors compared the CT data with densities in each finite element by relative difference measure. However, these works did not present the concept of minimizing the difference between the CT data and numerical solution to obtain an optimal configuration. One possibility, to determine the best configuration, would be based on a methodology that quantifies the sensitivity of a BR model in relation to the modification of

its parameters. This configuration can be determined by quantifying the sensitivity of a BR model concerning its parameters. Although they were not studying BR specifically, Rungsiyakull et al. (2010) used optimization and metamodeling to simulate the osseointegration process of a dental implant. The authors modified geometric parameters of the 2D model to maximize the interfacial stability between bone and implant.

We remark three important points of the studies discussed earlier. First, the bone density distributions are unique for each subject. Thus, the mentioned BR models result in qualitative comparisons. Second, modifying the parameters of a model generates different solutions. Also, the difference between the CT data and numerical solution can be quantified. Finally, from a set of solutions, a function that represents the approximate behavior of the response can be obtained. Thus, the present work aims to propose a new methodology for obtaining optimum parameters of BR models. The optimum parameters minimize the difference between the numerical and clinical density distributions bone. In this sense, we numerically characterized the femoral morphology of a given subject from his CT scan. For this, we implemented a computational structure using the Abaqus and Matlab packages. In this structure, we used the finite element method to stimulate the BR process with the parameters obtained via surrogate. We first tested the new methodology, and then we applied it to 18 subjects.

The text is organized as follows. Section 2 describes the materials and methods: solid model building, finite element models, the software packages used, the optimization problem, the BR model, and the surrogate. The Section 3 outlines the results. Initially, we validated the new methodology for one subject following by the application to the entire sample. We indicate the main aspects and the limitations of the present study in Section 4. Finally, the concluding remarks are shown in Section 5.

## 2. Materials and methods

### 2.1. The new methodology

#### 2.1.1. Solid model and density assignment

We followed the flowchart (Fig. 2a) to build the femoral solid model from a CT scan. That is, we loaded the DICOM images in the Invesalius software and obtained a femur surface, based on the bone tissue Hounsfield values (Opolski et al., 2014; Gomes et al., 2017; Souza et al., 2018, 2019). Then, we performed a surface treatment using the MeshMixer software (Upex et al., 2017; Arun et al., 2020; Burgade et al., 2020; Damon et al., 2020). Finally, the Solidworks transformed the bone surface into a solid. The MeshMixer step was useful for correcting issues and improving the surface quality before importing the surface into the Solidworks.

After building the femoral solid model, we employed two software packages for the density assignment. The first one was the Abaqus, where we discretized the solid into a finite element mesh, and generated the nodal coordinates and connectivity. The second software, Bonemat, assigned the clinical densities to the FEM model (Viceconti et al., 2004; Taddei et al., 2006; Laz et al., 2007; Schileo et al., 2007; Martelli et al., 2014). DICOM images, mesh connectivity, and nodal coordinates are the input data to the assignment process.

#### 2.1.2. Simulation of the bone remodeling process

We refer to Fig. 2b for the simulation of the BR process for a pre-established set of model parameters, which allowed us to obtain a numerical density distribution. For this, we used FEM via Abaqus software customized with a UMAT Fortran subroutine. This subroutine computes the elementary stress vector and has the equations of the BR model for analyzing the temporal bone behavior.

### 2.1.3. The general structure of the new methodology

The new methodology aims to find the optimal BR parameters for each subject. Thus, the optimal value can reduce the difference between numerical and CT density distributions. If it is possible to write a function that describes this difference, which we call relative difference of densities (*RDD*), we could apply an traditional optimization technique. These techniques allow obtaining the values of parameters of BR model that provide the minimum value of *RDD*. However, the function that describes the *RDD* is unknown, so we employed a surrogate. The surrogate provides an approximate response function for a set of input data. In this way, we can replace the real function by an analytical one that is easy to handle and approximate the response.

The surrogate quality depends on the design of experiments (DOE), which is a set of *np* starting points that aim to “fill” the design space. Each point has a set of parameters,  $x^{(i)}$ , which we used as input data to the BR model. The simulation via BR model gives the numerical density distribution,  $\rho(x^{(i)})$ , and we calculated the value of *RDD*. We defined the *RDD* between numerical and clinical distributions,  $\rho_{CT}$ , as

$$RDD^{(i)}[\%] = \frac{100}{\rho_c} \left[ \frac{1}{Nel} \sum_{j=1}^{Nel} \left( \rho^j(x^{(i)}) - \rho_{CT}^j \right)^2 \right]^{1/2}, \quad (1)$$

where *Nel* is the total number of finite elements in the mesh and  $\rho_c$  is the maximum cortical bone density value. The value obtained with this function, from the parameter set  $x^{(i)}$ , will compose the DOE. After performing the procedure for all *np* DOE points, we can build an initial response surface.

The surrogate allows obtaining an approximate function to the real one from a DOE. Generally, the initial data are not enough to represent satisfactorily the real function. Thus, we used an infill sampling criteria to improve the surface and to determine a new data point  $x^{(i)}$ . Then, we added this point to the DOE and generated a new response surface. We carried out this procedure until we obtained the optimum point. In this sense, this optimum point represents the set of parameters of BR model that best characterizes the numerical distribution regarding the CT scan. Fig. 2c presents the flowchart of the new methodology to determine the optimal values of parameters of BR model for each subject.

### 2.2. The main components of the new methodology

We can customize the new methodology for different DOE's, surrogates, and infill sampling criteria. Now, we specify the choice of the main components used in this study.

*Metamodel, DOE, and infill sampling and stopping criteria:* In the new methodology, we used the simple Kriging as a surrogate (Forrester et al., 2007, 2008; Roustant et al., 2013). In this, a given random process,  $Y(x)$ , is the sum of a known trend function,  $\mu(x)$ , and a centered random process,  $Z(x)$ . That is

$$Y(x) = \mu(x) + Z(x). \quad (2)$$

Also, with the Maximum Likelihood, we determinate the covariance kernel adjustment parameters (Forrester et al., 2008; Roustant et al., 2013). Thus, the  $Z(x)$  covariance is known.

The DOE used is the Latin Hypercube. In this DOE, we divide each variable into an equal number of points to be sampled. Yet, we ensure that each compartment contains a single orthogonal projection of the points. However, this characteristic alone is not enough to guarantee an adequate distribution of points in the design space. In this sense, we optimized the Latin Hypercube using the Morris–Mitchell criterion (Forrester et al., 2008; Roustant et al., 2013). The smaller the criterion value, the better will be the space-filling properties of the sample (Forrester et al., 2007).

We used the expected improvement as an infill criterion. In this criterion, we add new points,  $x^{(i)}$ , to the known ones so that the answer obtained from the surrogate is as close as possible to the real systems.

The choice of new points takes into account an improvement measure. Thus, when sampling a new point  $x^{(i)}$ , the improvement ( $I(x^{(i)})$ ) of the model is given by

$$I(x^{(i)}) = \begin{cases} y_{min} - y(x^{(i)}) & \text{if } y(x^{(i)}) < y_{min} \\ 0 & \text{if } y(x^{(i)}) \geq y_{min}, \end{cases} \quad (3)$$

where  $y(x^{(i)})$  is a function value of *RDD* found for the point added and  $y_{min}$  is lowest value of *RDD* obtained on the surrogate. However, the value of this improvement is not previously known, as  $y(x^{(i)})$  is unknown. The equation describing the expected improvement is

$$E[I(x^{(i)})] = \begin{cases} (y_{min} - \hat{y}(x^{(i)})) \Phi\left(\frac{y_{min} - \hat{y}(x^{(i)})}{\hat{s}(x^{(i)})}\right) & \text{if } \hat{s}(x^{(i)}) > 0 \\ +\hat{s}(x^{(i)}) \phi\left(\frac{y_{min} - \hat{y}(x^{(i)})}{\hat{s}(x^{(i)})}\right) & \text{if } \hat{s}(x^{(i)}) = 0. \\ 0 & \text{if } \hat{s}(x^{(i)}) = 0. \end{cases} \quad (4)$$

In Eq. (4),  $\hat{y}$  and  $\hat{s}^2$  are Kriging parameters, which represent, respectively, the prediction at an unsampled point and an error estimate of the model (Forrester et al., 2007). The parameter  $\Phi$  is the cumulative distribution function and  $\phi$  is the probability density function.

In this infill criterion, the expected improvement value is zero for known points. Another characteristic is the enhancement of the search in regions with little or no exploitation. The criterion value increases with the standard deviation between the approximate and analytical functions. Also, there is an increase in the criterion value in regions where the function average is low. Finally, there is no need to know the minimum value of the objective function (Forrester et al., 2008; Roustant et al., 2013).

In preliminary analyses (not presented), we noticed a high computational cost in the process of getting the value of *RDD* for each point of the DOE. Also, for these analyses, the surrogate generated from the DOE points exhibited a smooth behavior. For these reasons, we used the Latin Hypercube with 25 starting points for all simulations. Thus, we build the initial response surfaces from the quantification of the *RDD* for all these points that compose the DOE. After building the initial surrogate, we assessed whether two stopping criteria were satisfied: (a) the improvement of the objective function, *RDD*, in an interval of 5 iterations is fewer than 0.01%, and (b) the total number of points sampled must not exceed 100 points. If the analysis reaches any criterion, the optimum BR model parameters are found. Otherwise, the expected improvement infill criterion adds a new point and the optimization process continues. As a result of this new point, we built a new response surface. This process is maintained until the analysis reaches at least one of the stopping criteria.

**Bone remodeling model:** We use the Jacobs et al. (1995) BR model. This phenomenological model considers the bone tissue behaviors as linear, elastic, and isotropic. This model results in a density distribution that characterizes qualitatively the bone structure. Furthermore, the properties of bone tissue change according to stress and strain fields. The intensity of the stimulus at the tissue level  $\psi_t$  determines the bone response and is defined by

$$\psi_t = \left( \frac{\rho_t}{\rho} \right)^\gamma \psi \quad \text{being} \quad \psi = \sum_{i=1}^N (n_i \bar{\sigma}_i^{m_e})^{1/m_e}, \quad (5)$$

where,  $n_i$  is the average number of cycles per day of the load case  $i$ ,  $m_e$  is a weighting factor which establishes the relative importance between the effective stress magnitudes and number of loading cycles (Whalen et al., 1988),  $\rho_t$  is the density of cortical bone without porosity, determined by  $\rho_c/0.95$ ,  $\rho_c$  is the maximum density value of cortical bone and is equal to  $1.995 \text{ g/cm}^3$  (Doblaré and García, 2002),  $\bar{\sigma}_i$  is the effective stress in bone tissue at a continuous level, determined by the strain energy density and Young's modulus, and  $\gamma$  is the exponent of the

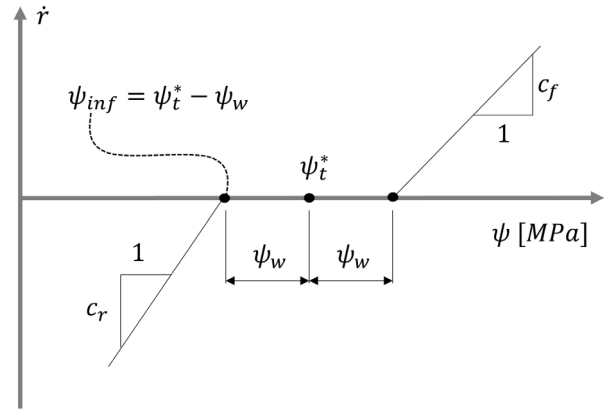


Fig. 3. Curve of the rate of remodeling ( $\dot{r}$ ) to present the parameters  $\psi_t^*$ ,  $\psi_w$ , and  $\psi_{inf}$ .

relationship between  $\psi_t$  and the mechanical stimulus at the continuous level ( $\psi$ ).

The stimulus  $\psi_t$  quantifies the tissue formation or resorption processes by a given reference value. Also, stimuli values close to the reference stimulus indicate an equilibrium condition in a region called lazy zone, of size  $2\psi_w$  (Carter, 1984). The authors delimited the lazy zone in the formulation of the BR model around the reference mechanical stimulus. In this region, there are no changes in the tissue properties, as seen in Fig. 3. The intensity of the stimulus  $\psi_t$  determines the response of the bone tissue to the applied load at a remodeling rate,  $\dot{r}$ , given by Jacobs et al. (1995)

$$\dot{r} = \begin{cases} c_r [\psi_t - (\psi_t^* - \psi_w)] & \text{if } \psi_t < (\psi_t^* - \psi_w), \\ 0 & \text{if } (\psi_t^* - \psi_w) \leq \psi_t \leq (\psi_t^* + \psi_w), \\ c_f [\psi_t - (\psi_t^* + \psi_w)] & \text{if } \psi_t > \psi_t^* + \psi_w. \end{cases} \quad (6)$$

The parameters  $c_f$  and  $c_r$  are empirical constant rates for bone formation and resorption, respectively. We considered the parameters  $c_r$  and  $c_f$  equals and they received the value of  $0.02 \text{ (\mu m/day)/(MPa/day)}$  (Beaupré et al., 1990).

The Young's modulus ( $E$ ) of bone tissue and Poisson's ratio ( $\nu$ ) are determined using the following experimental relationship

$$E(\rho) = b\rho^\beta = \begin{cases} 2014\rho^{2.5} & \text{if } \rho \leq 1,2 \text{ g/cm}^3, \\ 1763\rho^{3.2} & \text{if } \rho > 1,2 \text{ g/cm}^3, \end{cases} \quad (7)$$

and

$$\nu(\rho) = \begin{cases} 0,2 & \text{if } \rho \leq 1,2 \text{ g/cm}^3, \\ 0,32 & \text{if } \rho > 1,2 \text{ g/cm}^3, \end{cases} \quad (8)$$

respectively (Beaupré et al., 1990; Jacobs et al., 1995, 1997).

**Variables of the remodeling model applied in the methodology:** The BR model adopted has parameters that strongly influence the achievement of the final results of the simulations. We selected three empirical parameters to build the vector of design variables: (a) reference mechanical stimulus ( $\psi_t^*$ ), (b) the width of the lazy zone, and (c) exponent  $m_e$ . We carried out the analysis using two different approaches. In the first approach, the parameters considered were the lower limit ( $\psi_{inf}$ ) and the half-width of the lazy zone ( $\psi_w$ ). We defined the lower limit of the lazy zone as  $\psi_{inf}^* = \psi_t^* - \psi_w$  (Fig. 3). In the second approach, the parameters were the reference mechanical stimulus ( $\psi_t^*$ ) and the exponent  $m_e$ . We define the feasible region and the interval of each parameter based on preliminary analysis. Also, we considered the minimum point did not belong to the contour of that space. We present these ranges next.

The reference mechanical stimulus,  $\psi_t^*$ , represents the central point of the equilibrium region of the BR process. This parameter contributes to determining the rate of remodeling. In several studies, this parameter receives a value equal to  $50.0 \text{ MPa}$  (Beaupré et al., 1990; Jacobs et al.,

**Table 1**  
Information about the subjects used in this study.

Subject code	Gender	Age (years)	Body mass (kg)	Height (m)	Average number of steps by day
M41	F	44	96	1.65	4,000
M43	F	41	79	1.58	4,000
M44	F	46	82	1.60	4,000
M52	F	55	85	1.57	4,000
M53	F	54	82	1.59	4,000
M54	F	51	72	1.60	6,000
M61	F	67	60	1.60	4,000
M62	F	73	69	1.65	4,000
M64	F	81	80	1.68	4,000
H41	M	48	73	1.78	4,000
H42	M	49	79	1.80	4,000
H43	M	47	86	1.68	4,000
H51	M	53	120	1.68	4,000
H53	M	51	106	1.76	4,000
H54	M	52	78	1.74	6,000
H61	M	67	78	1.70	4,000
H62	M	66	75	1.78	4,000
H63	M	83	60	1.74	4,000

1995, 1997; Doblaré and García, 2002). However, in this work, we defined the reference mechanical stimulus as a feasible interval, limited by the values of 0.0 and 500.0 MPa.

The half-width of the lazy zone,  $\psi_w$ , delimits the equilibrium region of the model (Fig. 3). In general, studies defined this parameter as a percentage (25%) of the reference stimulus value ( $\psi_t^*$ ) (Jacobs et al., 1995, 1997; Doblaré and García, 2001, 2002). Here, we also defined the  $\psi_w$  as a feasible interval between 0.0 and 500.0 MPa. When we changed the  $\psi_w$  and  $\psi_t^*$  at the same time, part of the surrogate may become unfeasible. This happens when small values are assigned to the reference stimulus and high values to the lazy zone width. Furthermore, this can cause the lower limit of the equilibrium region ( $\psi_{inf}^*$ ) to assume negative values, which are physically unacceptable. To solve this issue, we used the  $\psi_{inf}^*$  as a design variable, replacing the reference mechanical stimulus ( $\psi_t^*$ ). We also defined this parameter as a feasible interval between the 0.0 and 500.0 MPa.

Finally, the last parameter is the exponent  $m_e$  (see Eq. (5)), which usually receives a value equal to 4. However, we defined this parameter as a feasible interval from 3 to 8 (Whalen et al., 1988; Beaupré et al., 1990; Jacobs et al., 1995).

**Optimization problem:** We have defined the objective function, the vector of design variables, and constraints. Now, we can present the optimization problems. These problems aim to identify the optimum values to parameters of the isotropic BR model proposed by Jacobs et al. (1995). We employed two approaches to describe the optimization problem. The first problem used has the vector of design variables  $x^{(i)}$  defined by the lower limit value of the lazy zone  $\psi_{inf}^*$  and its width  $\psi_w$ . We explicitly defined this problem as

$$\begin{aligned} & \text{minimize } RDD^{(i)}(\%) \\ & \text{subject to } 0.0 \leq x_1^{(i)} < 500.0 \text{ MPa} \\ & \quad 0.0 \leq x_2^{(i)} < 500.0 \text{ MPa} \end{aligned} \quad (9)$$

The second problem has the reference mechanical stimulus ( $\psi_t^*$ ) and the exponent  $m_e$  as design variables, and we defined it as

$$\begin{aligned} & \text{minimize } RDD^{(i)}(\%) \\ & \text{subject to } 0.0 \leq x_1^{(i)} < 500.0 \text{ MPa} \\ & \quad 3.0 \leq x_2^{(i)} < 8.0. \end{aligned} \quad (10)$$

**Description of the subjects information used in the analysis:** We used a sample of 18 subjects to apply the new methodology. The sample was divided into three age range: (a) from 40 to 49 years old, (b) from 50 to 59 years old, and (c) above 60 years old. Each age range had six subjects, divided equally between male (M) and female (F). The

subjects agreed to provide their CT files and answered a semi-structured questionnaire in an individual interview conducted at the Clinic Hospital Complex of Paraná (Curitiba - BR). It is important to note that we obtained all the questionnaire information from the subjects (Table 1). These procedures follows a project approved by the ethics committee with a Presentation Certificate for Ethical Appreciation (CAAE) number 76467917.0.0000.0096.

We defined the level of daily physical activity as the average number of steps in the walk and the questionnaire information. The subject informed the frequency of physical exercises for each week. The questionnaire allowed classifying the subjects into three categories: (a) sedentary, when the subjects did not perform physical activities, (b) lightly active, for those who walk once or twice a week, or (c) active for those who perform physical activities at least three times a week. According to Tudor-Locke et al. (2013), sedentary subjects have an average number of steps per day below 5000. Thus, we considered 4000, 6000, and 8000 steps per day for the sedentary, slightly active, and active subjects, respectively.

**Solid model build of the human femur from a CT scan.** We built the femur boundary surface from the CT scan using the software Invesalius. It was necessary to determine an appropriate range of Hounsfield values (HU) for the building process. We identified each region of the body, e.g., skin, internal organs, body fat, and bone, using a range of HU. For the bone tissue, this range presents a large variation (Adams et al., 2012). In this study, we considered the range between 200 and 2000 HU, which refers to trabecular and cortical bones, respectively. The femur has a thick layer of cortical bone along its surface. Thus, we could perform the solid model build using the HU range that characterizes the cortical bone. In some regions, the boundary surface identification can be difficult, due to the pixels size and the cortical bone thickness. Thus, the HU value is lower than the clinical one for these regions. To solve this problem, we used a wide range of HU values for the solid model building. A wide range can lead to obtaining a solid model with slightly larger dimensions than the real femur. Thereby, the femoral surface receives a density value smaller than the clinical one in the density assignment process. This difference occurs due to the different materials that compose the surface pixels. Therefore, we applied a scale factor of 95% to the solid model in the anteroposterior and medial-lateral directions (in the horizontal plane  $x - y$ ). The scale factor was not applied in the upper-lower direction ( $z$ -axis), since the CT scan images were generated orthogonal to this plane. This way, the measures between the slices do not suffer meaningful interference.

The densities assignment process to the solid model requires the utilization of calibration. We performed the calibration based on the proposed methodologies of Peng et al. (2006), Pérez et al. (2010), Pérez

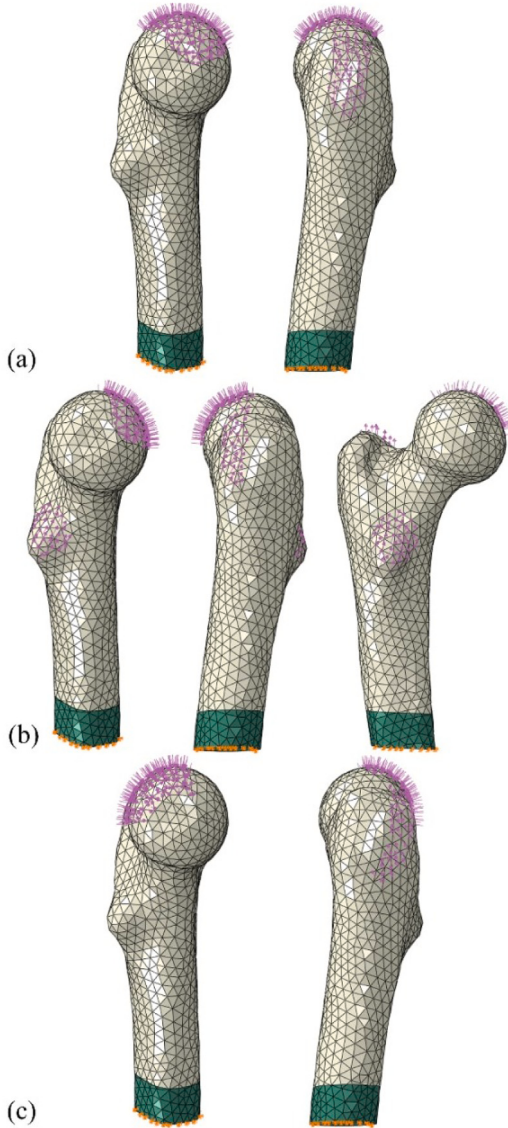


**Fig. 4.** Loading condition applied on the femur described by (a) touch of the foot on the floor, (b) flexion, and (c) extension.

and Seral-García (2013), and Pérez et al. (2014). Pérez and Seral-García (2013) obtained the density values using

$$\rho_{el} = 1 + 0.0007185 HU. \quad (11)$$

We employed Eq. (11) to transform the HU values to density, with the following premises (a) the cortical bone with null porosity has a density value of  $2.1 \text{ g/cm}^3$  (Doblaré and García, 2002); (b) the density of water is equal to  $1.0 \text{ g/cm}^3$ ; (c) the porosity of cortical bone varies between 5.0% and 30.0% (Hall, 2007); (d) the porosity of trabecular bone varies between 30.0% and 90.0% (Hall, 2007) and; (e) a fluid material fills porosity of the bone tissue with a density value similar to the water.

With these considerations, the density value obtained from the CT scan should vary between  $1.11$  and  $2.045 \text{ g/cm}^3$ . Values below this range were changed to  $1.11 \text{ g/cm}^3$ . Similarly, values above the range were changed to  $2.045 \text{ g/cm}^3$ .

In the BR simulations, we did not consider the densities referent to the fluid materials. In general, the works considered the concept of apparent density (Jacobs et al., 1995, 1997; Doblaré and García, 2001, 2002). We obtained the apparent density value with a CT scan

**Table 2**

Characteristics of the finite element mesh.

Subject code	Element type	Nodes	Elements
F54	C3D10	161,986	112,229
Subject code	Element type	Nodes	Elements
F41	C3D4	20,721	107,358
F43	C3D4	18,584	96,648
F44	C3D4	17,125	92,184
F52	C3D4	19,031	99,032
F53	C3D4	18,217	94,452
F54	C3D4	18,192	94,397
F61	C3D4	18,889	98,018
F62	C3D4	19,750	102,909
F64	C3D4	20,646	107,805
M41	C3D4	20,417	106,653
M42	C3D4	19,369	100,866
M43	C3D4	20,328	105,589
M51	C3D4	20,623	107,708
M53	C3D4	18,201	94,721
M54	C3D4	18,201	94,721
M61	C3D4	16,782	86,008
M62	C3D4	20,033	104,450
M63	C3D4	22,691	117,958

and assigned it to each finite element of the mesh. Thus, the apparent density is given, through the mixing rule, by

$$\rho = \frac{\rho_{el} - \rho_{H_2O}}{\rho_c - \rho_{H_2O}} \rho_c, \quad (12)$$

where  $\rho_{el}$  is the density value obtained using the Bonemat software and  $\rho_{H_2O}$  is the density of water.

Despite the utilization of a scale factor of 95% in the femur model, the density field is not similar to the clinical distribution. The boundary of the actual femur has cortical tissue, which presents high densities. The boundary of the solid model showed regions with lower densities values when compared to the CT scan. The reason can be the composition of the pixels of the boundary. In these regions, there is a mixture of different materials, e.g., bone, muscle, and cartilage. Thus, the boundary pixels have an intermediate value. In this way, we identified and listed all nodes localized at the boundary surface of the bone and all elements connected to each one of these nodes. Thus, we formed patterns of associated elements for each node. Each element of that list received the largest density value found between the elements that belong to the pattern.

*Finite element model.* In the simulations, we employed geometric models for the left femurs of each subject presented in Table 1. Each geometric model contains the femoral proximal region and part of the diaphysis. The size model is approximately 150 mm.

The FEM analyses of the BR problems can present a phenomenon called checkerboard. This phenomenon appears due to an exponential relation between the density and elastic modulus of the tissue. The occurrence of this oscillatory pattern results in solutions with poor quality and a strong mesh dependence (Weinans et al., 1992; Jacobs et al., 1995; Calvo-Gallego et al., 2021). Therefore, we employed two approaches to mitigate the checkerboard formation: (a) tetrahedral finite elements with quadratic displacement field, C3D10 (Bendsøe and Sigmund, 2003; Kowalczyk, 2010); and (b) tetrahedral finite elements with linear displacement field, C3D4, associated with stress field smoothing by nodal average (Ashrafi et al., 2020; Dicati et al., 2020; Gubaua et al., 2020). Table 2 presents the information regarding the finite element mesh for each geometric model.

Usually, the loading condition applied to the femur model corresponds to a gait cycle (Jacobs et al., 1995; Doblaré and García, 2001; Saeidi et al., 2019; Ashrafi et al., 2020; Dicati et al., 2020; Gubaua et al., 2020). We defined the loading condition (Fig. 4) by forces derived from two main sources: (a) compression on the femoral head due to the contact with the acetabulum; and (b) traction forces

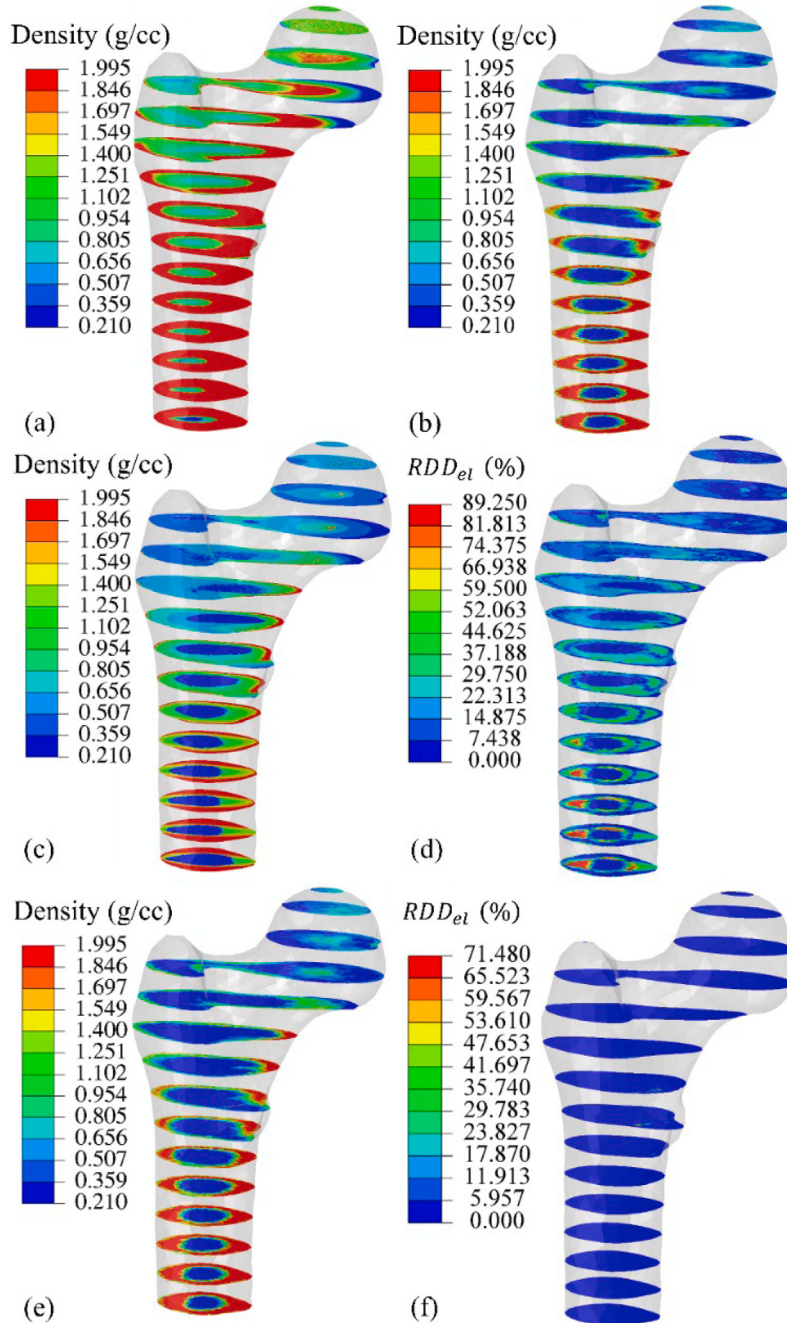


**Fig. 5.** Results for subject F54: (a) density distributions for the original model of Jacobs et al. (1995) with the reference parameters, (b) density distribution from CT scan, (c) density distribution using the optimum parameters in analysis with the homogeneous initial distribution, (d) elementary RDD distribution for analysis with the homogeneous initial density distribution, (e) density distribution for optimum parameters in analysis with initial density distribution from CT scan, and (f) elementary RDD distribution for analysis with initial density distribution from CT scan.

due to the muscle reactions. Thus, the loading condition has three distinct instants, which correspond to flexion, touch of the feet on the floor, and extension of the lower limb. We applied the forces in pairs, being the compression and traction on the femoral head and greater trochanter, respectively. An exception is the flexion movement, where there is a traction force applied on the lesser trochanter. The load values for the femoral head and greater trochanter may be seen in Beaupré et al. (1990), while Greenwald and Haynes (1972) proposed the areas of distribution of the compression loads. Bagge (1999) presented the directions and areas for loads on the greater trochanter. Finally,

the loading condition on the lesser trochanter followed Simões et al. (2000).

Table 3 shows the intensities and directions of the load applied to the femur for a 70 kg subject. We linearized the intensity of the loads (Table 3) to correspond to the body mass of each subject (Table 1). We applied homogeneous Dirichlet boundary conditions to a small solid inserted into the mid-portion of the femoral diaphysis with elastic, linear, and isotropic behavior. This solid prevents stress concentration in the femur model.

**Table 3**

Load	Movement	Intensity (N)	Direction <sup>a</sup>
Compression-1	Fig. 4a	1,158	Pressure (normal to the surface)
Compression-2	Fig. 4b	2,317	Pressure (normal to the surface)
Compression-3	Fig. 4c	1,548	Pressure (normal to the surface)
Traction-1	Fig. 4a	351	-0.1490; 0.06241; 0.9869
Traction-2	Fig. 4b	703	0.3827; 0.4073; 0.8292
Traction-3	Fig. 4c	468	0.3232; -0.3878; 0.8632
Traction-4	Fig. 4b	188	0.1564; 1.6696; 0.7314

<sup>a</sup>Coordinate system is orientated with x-axis in lateral-medial direction, y-axis anterior-posterior direction, and z-axis for lower-upper direction.

### 3. Results

#### 3.1. Validation of the new methodology

The initial results aim to verify the new methodology and understand the influence of the parameters on the BR process. We used two different density distributions to start the BR analyses to assess the sensitivity to the initial guess: homogeneous of 0.50 g/cm<sup>3</sup> (Jacobs et al., 1995, 1997; Doblaré and García, 2001, 2002) and the one from CT scan. In these analyses, we randomly chosen the subject F54. In the first analysis, we used the half-width of the lazy zone ( $\psi_w$ ) and the lower limit of this region ( $\psi_{inf}^*$ ) as design variables (see the first optimization problem). As we indicated before, the quadratic elements C3D10 discretizes the femur geometry (Table 2).

We observed that the density distributions using the optimum parameters presented several discrepancies (Figs. 5 and 6). The online resources ESM1.mp4 and ESM2.mp4 present the evolution of the response surfaces for the analyses started from the homogeneous and CT scan density distributions, respectively. In the analysis with the homogeneous initial distribution, the results of the design variables were:  $\psi_{inf}^* = 181.04$  MPa,  $\psi_w = 120.11$  MPa, and  $RDD = 21.42\%$ . In the analysis with the initial distribution obtained using the CT scan, the values were 16.17 MPa, 500.0 MPa, and 1.15%, for the same parameters. The main reason for these differences is the regarding of the lazy zone. As indicated by Klarbring and Torstenfelt (2012), Martínez-Reina et al. (2016) and, Dicati et al. (2020), the lazy zone leads to results dependent on the initial distribution. In this case, the lazy zone and the CT scan initial distribution make the new methodology vicious. The algorithm searches parameters that do not produce variation in the density distribution at the final solution. Fig. 5f shows this non-variation behavior by presenting the elementary RDD between the numerical (Fig. 5e) and CT scan (Fig. 5b) density distributions. Thus, the lowest and the biggest possible values of, respectively,  $\psi_{inf}^*$  and  $\psi_w$  composes the feasible set of parameters. So, the following BR analyses consider the lazy zone described by a point, that is, null width (Fig. 3 with  $\psi_w$  equal to 0).

In the initial results, we also evaluated the formation of the checkerboard pattern. One can note the quadratic elements did not completely inhibit the pattern formation (Fig. 5). Furthermore, we verify the mass variation during the analysis. The analysis with the homogeneous initial density distribution still presents changes at the end of the simulation (Fig. 7). Therefore, we observed a meaningful difference between the values of total bone mass in the analysis that considered the lazy zone (Fig. 7).

We adopted the modifications proposed by Dicati et al. (2020) for the Jacobs et al. (1995)' BR model. The modifications remove the dependency of the initial density distribution and refer to (a) change the rate of remodeling curve into the lazy zone region; (b) define the transition functions to guarantee the continuity of the expressions to Young's modulus (Eq. (7)) and Poisson's ratio (Eq. (8)); (c) adapt the exponents used in the equations of the elastic modulus (Eq. (7)) and the mechanical stimulus (Eq. (5)); and (d) use a control technique to

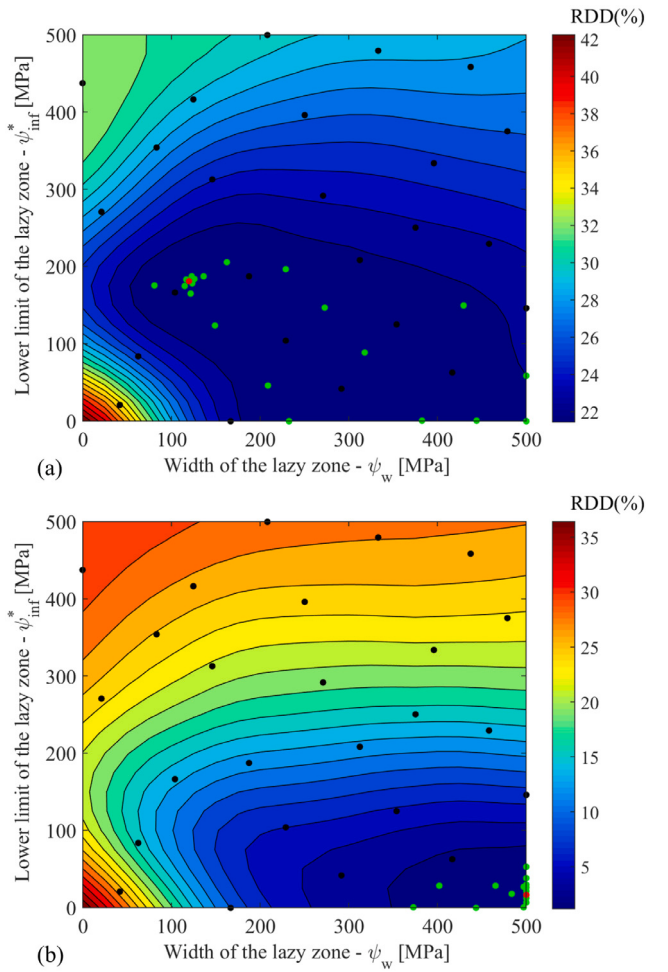


**Fig. 6.** Response surfaces for analysis of the F54 subject. Response surface for analysis started with (a) the homogeneous and (b) CT scan density distributions. The black points refer to DOE. The green points were added using the expected improvement infill criterion. And, finally, the red points indicate the optimum value of the RDD. (For interpretation of the references to color in this figure legend, the reader is referred to the web version of this article.)

inhibit the checkerboard formation. To solve this, we used the stress field smoothing by nodal average (Ashrafi et al., 2020; Dicati et al., 2020; Gubaua et al., 2020).

After the modifications, we performed two numerical analyses. Again, we used the femoral geometry of the subject F54 and the same initial density distributions: homogeneous distribution of 0.5 g/cm<sup>3</sup> (Jacobs et al., 1995, 1997; Doblaré and García, 2001, 2002), and the one from CT scan. Furthermore, we performed simulations with 500 iterations. In both analyses, we used the reference mechanical stimulus ( $y_t^*$ ) and the exponent  $m_e$  as design variables (see the second optimization problem). We observed that the response surfaces for both simulations are visually similar (Fig. 8). See the online resources ESM3.mp4 and ESM4.mp4 for visualizing the evolution of the response surfaces for the analyses started from the homogeneous and CT scan initial density distributions, respectively. On these response surfaces (Fig. 8a and 8b), the 25 black points refer to DOE. In the analysis with homogeneous initial density distributions, the surrogates received 80 green points (Fig. 8a). In the other analysis, the surrogate received 22 green points (Fig. 8b). The expected improvement infill criterion defines the application of the new points. Finally, the red point indicates the optimum value of the optimized function.

The RDD data (Table 4) indicate a meaningful improvement when we compared the density distributions obtained with the optimum parameters (Fig. 9c and 9e) and with the parameters indicated by Jacobs

**Table 4**  
Optimum parameters and *RDD* obtained with the new methodology for subject F54.

BR model	Initial density distribution (g/cm <sup>3</sup> )	$\psi_t^*$ (MPa)	$m_e$	<i>RDD</i> (%)
Modified model	0.50 (homogeneous)	403.507	4.158	16.482
Modified model	CT scan (heterogeneous)	395.106	4.287	16.401
Original model Jacobs et al. (1995) <sup>a</sup>	0.50 (homogeneous)	50.0	4.0	44.846

<sup>a</sup>Use of BR model with the parameters presented in its publication.

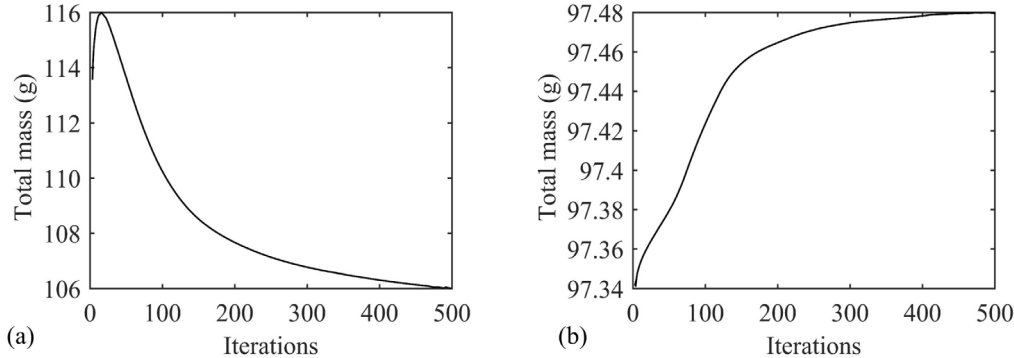


**Fig. 7.** Total mass variation of the femur in analysis with the quadratic tetrahedral finite element. Graphics of analysis started with the (a) homogeneous, and (b) CT scan density distributions.

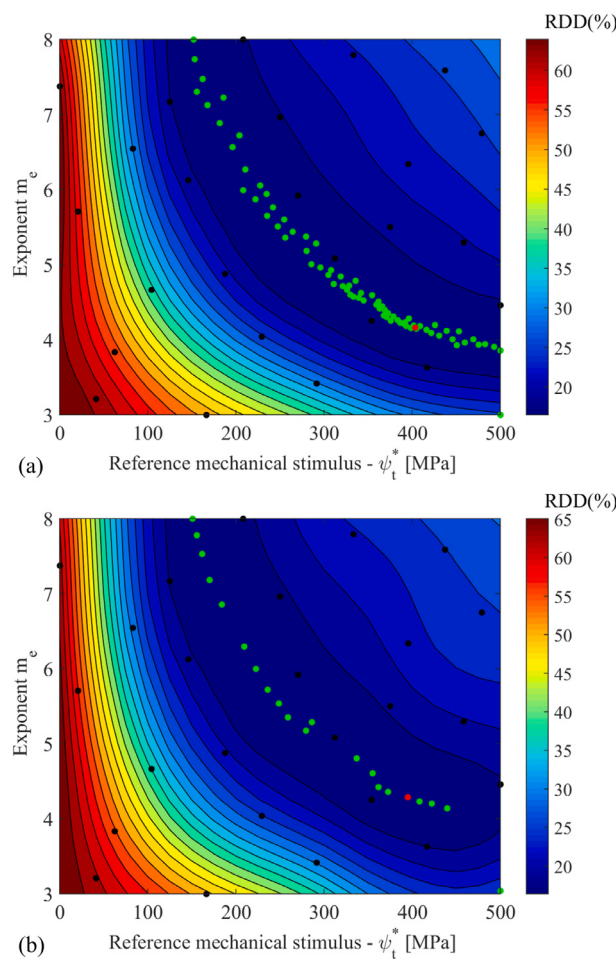


**Fig. 8.** Response surfaces for analysis of the F54 subject. Response surface for analysis started with (a) the homogeneous and (b) CT scan density distributions. The black points refer to DOE. The green points were added using the expected improvement infill criterion. Finally, the red points indicate the optimum values of the *RDD*. (For interpretation of the references to color in this figure legend, the reader is referred to the web version of this article.)

et al. (1995) (Fig. 9a). This improvement corresponds to a reduction of approximately 63% in the *RDD* value. Besides, one can note the values obtained for  $\psi_t^*$  are eight times higher than the standard value. The increase of  $\psi_t^*$  occurs due to the use of equal exponents in the equations of the tissue level mechanical stimulus (Eq. (5)) and elastic modulus (Eq. (7)). In its turn, the exponent  $m_e$  weights the relative importance of the stress magnitude for the number of cycles applied. The increase in the exponent indicates the greater importance of activities that generate high stress at the bone site. The walk is the activity performed by the subjects used in this study. For this activity, the exponent indicated in the literature would be equal to 4, which is very close to the values presented in Table 4.

The density distributions obtained with the optimum parameters are similar (Fig. 9c and 9e). Therefore, we can see a tendency to the uniqueness of results. Table 4 presents the optimum parameters obtained with the new methodology. The idea is that the density distributions come as close as possible to the CT distribution (Fig. 9b). Thus, one can note a trend convergence of results similar in the total mass history of the femur (Fig. 10). For both simulations, the value of the total mass is approximately 107 g. We can also see in the density distributions (Fig. 9c and 9e) the main aspects of the femoral morphology as the cortical bone formation around the femoral diaphysis, the medullar cavity formation, the distribution of trabecular density along with the femoral head, and Ward's triangle formation at the femoral neck.

The results show that the new methodology needs a BR model that is independent of the initial conditions. That is, the solution must tend to uniqueness. The differences in the final density distributions (Fig. 9c and 9e) occur due to the number of increments considered in the BR process analysis. The homogeneous initial distribution (Fig. 9c) needs more time to get the same final result of the one with initial density distribution from the CT scan (Fig. 9e).

### 3.2. Application of the new methodology to obtain optimum parameters of BR model to all subjects

We applied the new methodology to 18 subjects (Table 2). In these analyses, we also used the Jacobs et al. (1995)'s BR model with the Dicati et al. (2020)'s modifications. The mass convergence curves (Fig. 10) are stable after 500 iterations. We kept this total number of iterations for all analyses, which started with the density distributions from the CT scan of each subject. Finally, we used as

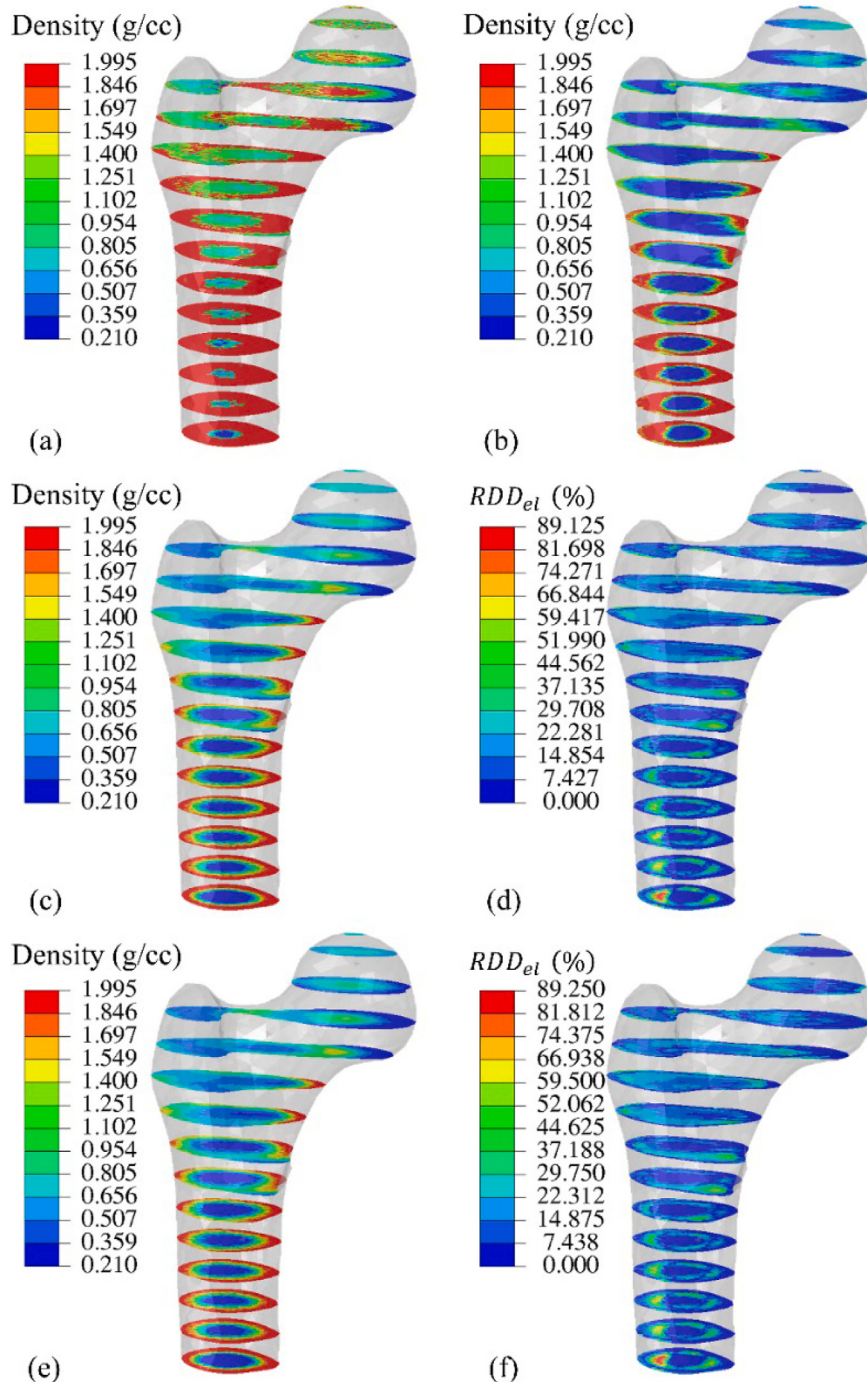


**Fig. 9.** Results for subject F54: (a) density distributions for the original model of Jacobs et al. (1995) with the reference parameters, (b) density distribution from CT scan, (c) density distribution using the optimum parameters in analysis with the homogeneous initial distribution, (d) elementary RDD distribution for analysis with the homogeneous initial density distribution; (e) density distribution for optimum parameters in analysis with initial density distribution from CT scan, and (f) elementary RDD distribution for analysis with initial density distribution from CT scan.

parameters the reference mechanical stimulus ( $\psi_t^*$ ) and the exponent  $m_e$  (see the second optimization problem). The online resources ESM5.jpg, ESM6.jpg, ESM7.jpg, ESM8.jpg, ESM9.jpg, and ESM10.jpg show the density distributions obtained for each subject.

Table 5 presents the optimum parameters obtained using the surrogate and its respective RDD values regarding the CT. The entire sample presented mean and standard deviation values to the  $\psi_t^*$  and exponent  $m_e$  of  $370.361 \pm 134.50$  MPa and  $4.92 \pm 1.47$ , respectively. We also evaluated the results by dividing the sample by gender. The female (F) subjects presented the values of  $\psi_t^*$ ,  $m_e$ , and RDD were  $417.02 \pm 106.55$

MPa,  $4.67 \pm 1.21$ , and  $16.48 \pm 4.14\%$ , respectively. The male (M) subjects presented values of  $323.70 \pm 143.08$  MPa,  $5.17 \pm 1.65$  and  $17.44 \pm 1.74\%$ , for  $\psi_t^*$ , the exponent  $m_e$  and RDD, respectively. In the results shown in Table 5, three main sources have effects on the results presented. The first factor is geometric, where the intensity of the loads and the geometry of the bone are individualized. The second factor is associated with the BR model, where we insert information about the intensity of physical activity. Furthermore, we optimized the model parameters for obtaining a more realistic bone density distribution and close to the CT scan. And, the third factor is the CT scan. The CT scan is

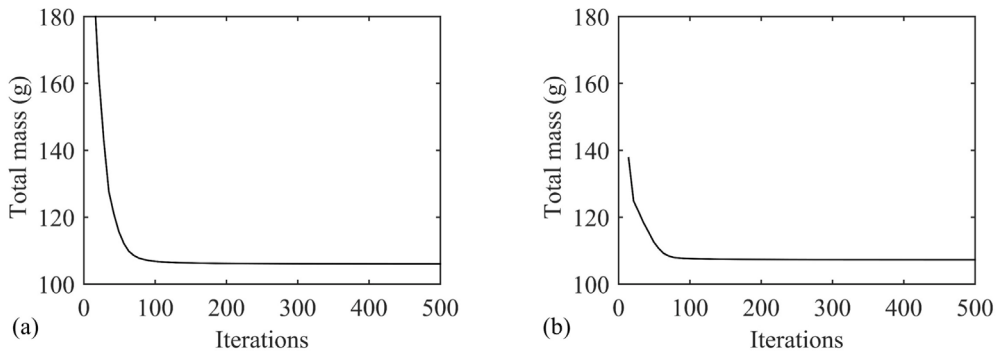


**Fig. 10.** Total mass variation of the femur in analysis. Graphs of the analysis started with the (a) homogeneous and (b) CT scan density distributions.

**Table 5**

Optimum parameters and *RDD* for each subject obtained in the response surfaces.

Subject	$\psi_t^*$ (MPa)	$m_e$	<i>RDD</i> (%)
F41	421.972	3.833	16.872
F43	363.521	4.403	16.223
F44	490.217	4.402	14.360
F52	489.513	4.246	17.559
F53	490.535	4.111	17.491
F54	395.106	4.287	16.401
F61	143.462	8.000	15.581
F62	488.277	4.251	18.281
F64	470.611	4.837	15.582
M41	498.720	3.288	19.431
M42	151.196	7.089	17.410
M43	152.953	7.588	17.145
M51	455.136	4.058	19.238
M53	416.667	3.625	18.454
M54	467.463	4.536	13.987
M61	132.222	7.478	19.079
M62	240.889	5.174	16.786
M63	408.037	3.711	15.442

the direct information about each subject. So, we implicitly considered the aspects: age, gender, and effect of body mass. Those aspects have a significant influence on the numerical results.

We observe that a significant number of points inserted by the infill criterion presented a difference of 1.0% or less in *RDD* values, compare to the *RDD* optimum point. Then, we plotted these points for all subjects (Figs. 11 and 12), and we observed similar behavior in the design variable space (parameters of BR model). Thus, one can note a region of optimum values, since the *RDD* values are very similar, instead of only one optimum point. This region presents a tendency to approach a hyperbola.

We assembled the data presented in Figs. 11 and 12, according to the age range and gender. Thus, we analyzed the behavior of the values obtained for each group of subjects (Fig. 13). In Fig. 13, the numbers 4, 5, and 6 indicate the age range from 40 to 49, 50 to 59, and above 60 years old, respectively. We performed other analyses using the values obtained for the entire sample, differentiating by the female (F) and male (M) (Fig. 14). For each one of the distributions, we proposed a curve of tendency given by

$$m = A\psi_t^{*-a}, \quad (13)$$

where  $A$  and  $a$  are the coefficients of each one of the curves, as shown in Table 6. The  $R^2$  values indicate the quality of the fit obtained.

#### 4. Discussions

We showed that the BR model must not be dependent on the initial density distribution. The lazy zone defined as an equilibrium region by Carter (1984) leads the simulation to different solutions. Beyond the dead zone, the Dicati et al. (2020)'s modifications and effective control

**Table 6**  
Coefficients and  $R^2$  of each trend curve.

Subject groups	Figure	$A$	$\alpha$	$R^2$
H4	13a	118.64	0.579	0.905
H5	13c	83.63	0.499	0.698
H6	13e	132.73	0.593	0.968
H	14a	97.22	0.534	0.842
M4	13b	109.15	0.539	0.912
M5	13d	119.07	0.543	0.910
M6	13f	75.40	0.460	0.795
M	14b	92.06	0.500	0.834

of the checkerboard (Ashrafi et al., 2020; Dicati et al., 2020; Gubaua et al., 2020) are required for uniqueness.

The checkerboard occurs due to the exponential relation between Young's modulus and density. We can define the pattern as a search for the density distribution that presents the highest possible stiffness. In this sense, we mitigate the checkerboard pattern by smoothing the stress field (Ashrafi et al., 2020; Dicati et al., 2020; Gubaua et al., 2020). Thus, the elements have lower density values than the distribution with the checkerboard pattern. This is also valid for the original Jacobs et al. (1995)'s BR model (Fig. 9a). In this distribution, we observe that there is no medullar cavity formation inside the femoral diaphysis. However, the morphological structure of the human femur is well represented in the density distributions of Fig. 9c and 9e. Thus, one can note the improvement of the new methodology by comparing Fig. 9c and 9e with Fig. 9a. Therefore, the improvement referent to subject F54 is evident and quantified through *RDD*.

We observed that most of the elements presented low *RDD* values along the femur of the subject F54. However, one can note intermediary *RDD* values in the trabecular tissue in the greater trochanter, femoral head, and femoral neck. The highest *RDD* values are in regions of transition between cortical and trabecular tissues at the diaphysis and lesser trochanter. These high values appear even with the use of traction load that characterizes the iliopsoas muscle. Those aspects occurred due to the loading condition. The loads represent a specific condition that happens during the walk. Besides, we used a small number of thigh and hip muscles to characterize the loading at the region. A realistic definition of the load condition is important in BR simulations with phenomenological models. For this kind of BR model, the bone tissue behavior is associated with the mechanical stimulus. Still, few points presented elevated *RDD* level in the distributions (Fig. 9d and 9f).

The response surface of all subjects in the sample (not presented in this paper) follow the same behavior showed in Fig. 8. There is a region of minimum behavior of the function within the restrictions imposed on the optimization problem used in the study. This region presents a hyperbola behavior. Thus, there are several points with the

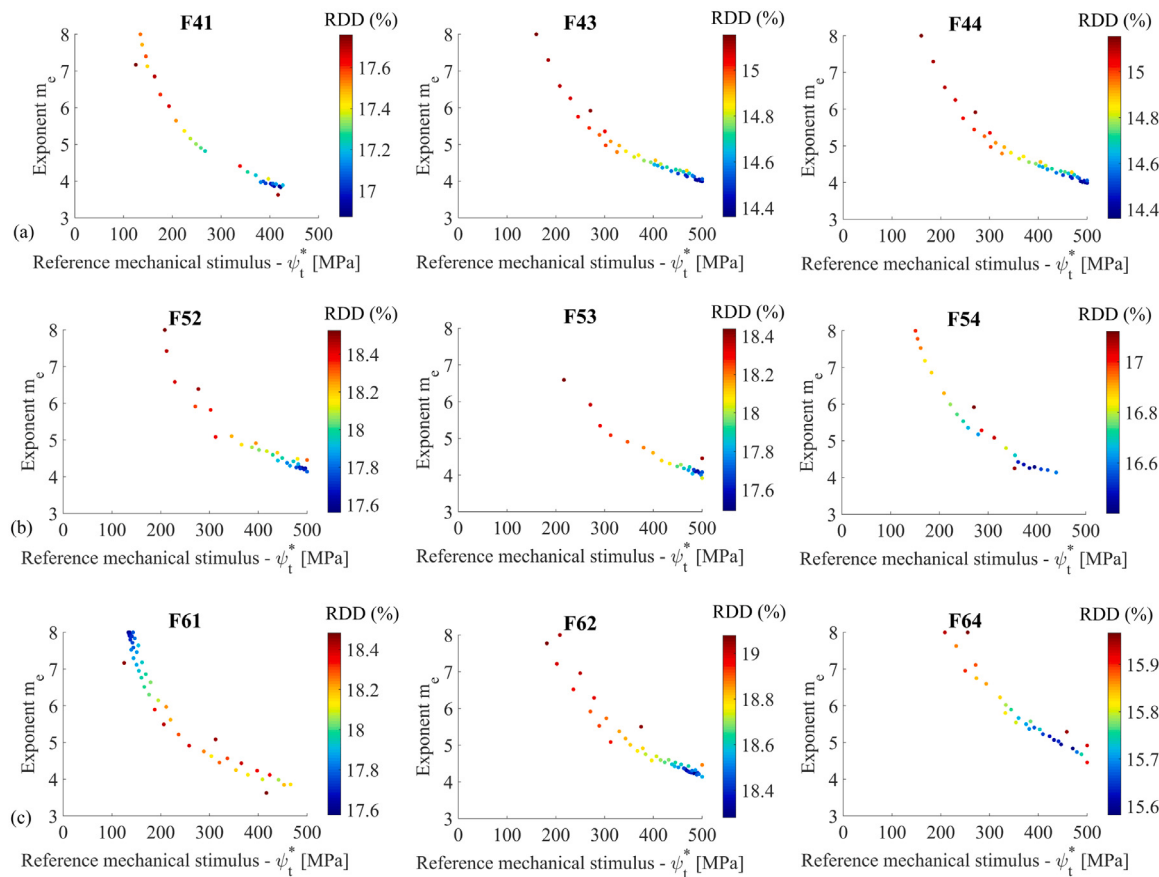


**Fig. 11.** Surrogate points that present a difference less than 1.0% in the *RDD* concerning the optimum point. Female (F) subjects in the age range from (a) 40 to 49, (b) 50 to 59, and (c) above to 60 years old.

potential to be the optimum value. The surrogate behavior explains the distinct values for optimal parameters among subjects. The subject F61 presented values of  $\psi_t^*$  and the exponent  $m_e$  equal to 143.462 MPa and 8, respectively, and even so, presented a *RDD* of 15.581%. Subjects M42, M43, M61, and M62 present the same behavior and *RDD* values of 17.410%, 17.145%, 19.079%, and 16.786%, respectively.

We obtained higher values of the reference mechanical stimulus ( $\psi_t^*$ ) compared to values proposed by Jacobs et al. (1995). We got a value of  $370.361 \pm 134.50$  MPa for the sampled subjects (Table 5). This difference in ( $\psi_t^*$ ) values occurred due to the Dicati et al. (2020)'s modifications used in BR formulation. We evaluate the *RDD* values by separating the sample by gender. The male subjects presented a reference mechanical stimulus lower than the female subjects ( $323.70 \pm 143.08$  MPa and  $417.024 \pm 106.548$  MPa, respectively). However, this difference is not meaningful due to the elevated values of standard deviation. The difference between the  $\psi_t^*$  values occurs due to the body mass. The male sample has a body mass higher than the female, with an average value of 83.9 and 78.3 kg, respectively. Low values of  $\psi_t^*$  allow more bone tissue formation.

The exponent  $m_e$  presents a contrary behavior being higher for male than female subjects ( $5.172 \pm 1.65$  and  $4.665 \pm 1.207$ , respectively). However, this difference is not significant. Such exponent quantifies the relative importance of the stress magnitude for the number of cycles applied (Whalen et al., 1988; Beaupré et al., 1990; Jacobs et al., 1995).

The new methodology was based on the combination of surrogates, DOE, FEM, and the BR model. This combination leads to several limitations, being the most important the following:

- (1) The acquisition of the 3D geometry of the human femur. We used the filtering function, called *bone*, to build the solid model

in the Invesalius software. As described before, the interval of Hounsfield values for this filter is considerably large. In this way, the femoral boundary exceeds the limits of the bone in the tomography. To fix it, we used an empirically determined scale factor of 0.95 in the *x* and *y* directions (anteroposterior and lateral-medial, respectively) of the femur geometry.

- (2) CT calibration using the data from the literature. Since we developed a quantitative study, the ideal would be the use of a phantom.
- (3) The process of recovering the density distribution of computed tomography. We carry out this process by mapping all the pixels that belong to the built bone. We used BoneMat software to do this. Some rectangular pixels are not effective for representing femoral geometry in some regions. For example, in the boundary surface or where there is a transition between cortical and trabecular tissues. Besides, the pixel at the boundary region can represent different materials (e.g., bone, muscle, and cartilage). Thus, we determined the assigned property from a weighted average of the material properties that compose this pixel. We use this weight value to assign the property to the finite element. If the finite element is larger than pixels, we performed a weighted average between the pixels that compose each finite element. Thus, the boundary and the transition region between cortical and trabecular at diaphysis receive the properties with averaged values. Therefore, the elementary *RDD* value is amplified. Still, regarding the recovery process of the density distribution, we used the BoneMat software. This software requires the user to position the finite element model on the CT scan. This positioning is dependent on the user, which can lead to a less precise result.

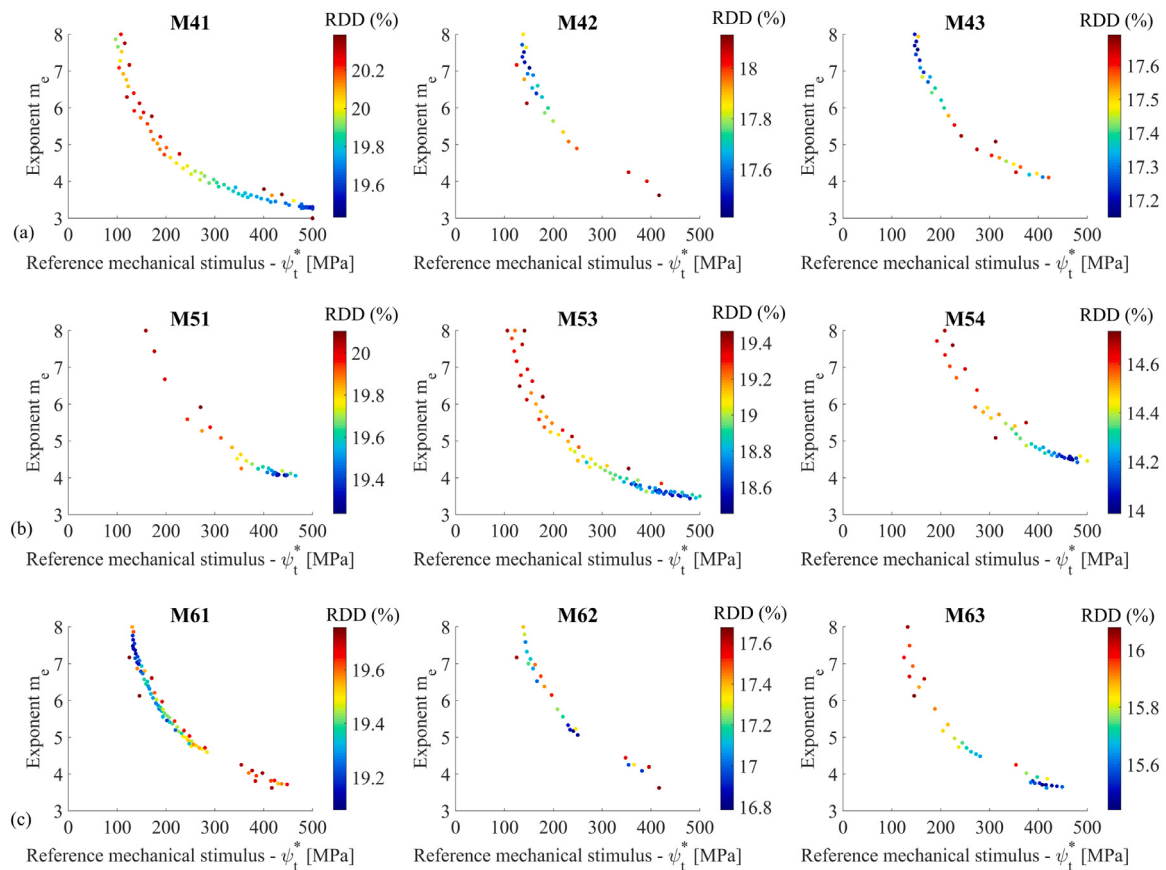


**Fig. 12.** Surrogate points that present a difference less than 1.0% in the RDD concerning the optimum point. Male (M) subjects in the age range from (a) 40 to 49, (b) 50 to 59, and (c) above to 60 years old.

- (4) The application of the loading condition. The loading condition is unique as well as the density distribution. Each subject has an area for loading application, intensity, and orientation. Besides that, these parameters vary according to the type of physical activity. We used the loading condition only with the loads that act on a gait cycle, and not all the muscles involved were considered.
- (5) In this study, we linearized the intensities of the load condition applied on a subject weighing 70 kg to determining the load intensities for each subject. An experimental determination of the load intensities and their regions for application would contribute even more to the accuracy of the simulations concerning the clinical data.
- (6) There was no differentiation between the trabecular and cortical tissues. Such tissues present distinct properties and a totally different structure (Doblaré et al., 2004; Rüberg et al., 2005; Martínez-Reina et al., 2009). However, we assigned to the bone tissue unique values for  $\psi_t^*$  and for the exponent  $m_e$  without a clear distinction. We followed Jacobs et al. (1995) that used the same consideration.
- (7) We used only one BR model, which is isotropic and phenomenological. More robust models, as the anisotropic model developed by Doblaré and García (2002) or chemomechanobiological models (Rüberg et al., 2005; Ashrafi et al., 2020, 2021), could provide better results. Still, they could allow to input other constants in the optimization process.
- (8) About the sample used. We used a small number of subjects and not employed any information about individuals of the range from 20 to 29 and 30 to 39 years old.

## 5. Conclusions

We presented a new methodology to predict bone tissue behavior by individualizing Jacobs et al. (1995)'s BR model. Although the limitations due to the several complexities of the human body as, for example, the area for load application on the femur, the methodology allowed obtaining a more accurate and realistic bone density distribution for each subject. Here, the adoption of numerical tools (surrogate, DOE, and FEM) allowed obtaining specific parameters by considering physical aspects as the body mass and daily physical activity, and the density distributions.

For the new methodology to have a good performance, it is necessary to use a BR model not dependent on the initial density distribution. This dependence is a characteristic of models that use the lazy zone in their formulation and the Jacobs et al. (1995)' BR model is one of them. We adopted the Dicati et al. (2020)'s modifications to solve it. The modified BR model allowed getting an improvement in the RDD value. The density distributions obtained with optimum parameters improved 50% the RDD value compared with the distribution obtained using the original parameters of BR model (Jacobs et al., 1995).

Finally, we can assert that the new methodology presents satisfactory results despite the limitations and simplifications. The new methodology decreased the difference between the numerical and clinical density distributions. Furthermore, the results allowed visualizing the differences between the clinical distributions. Thus, it is not possible to use the same parameters for all subjects in a detailed analysis.

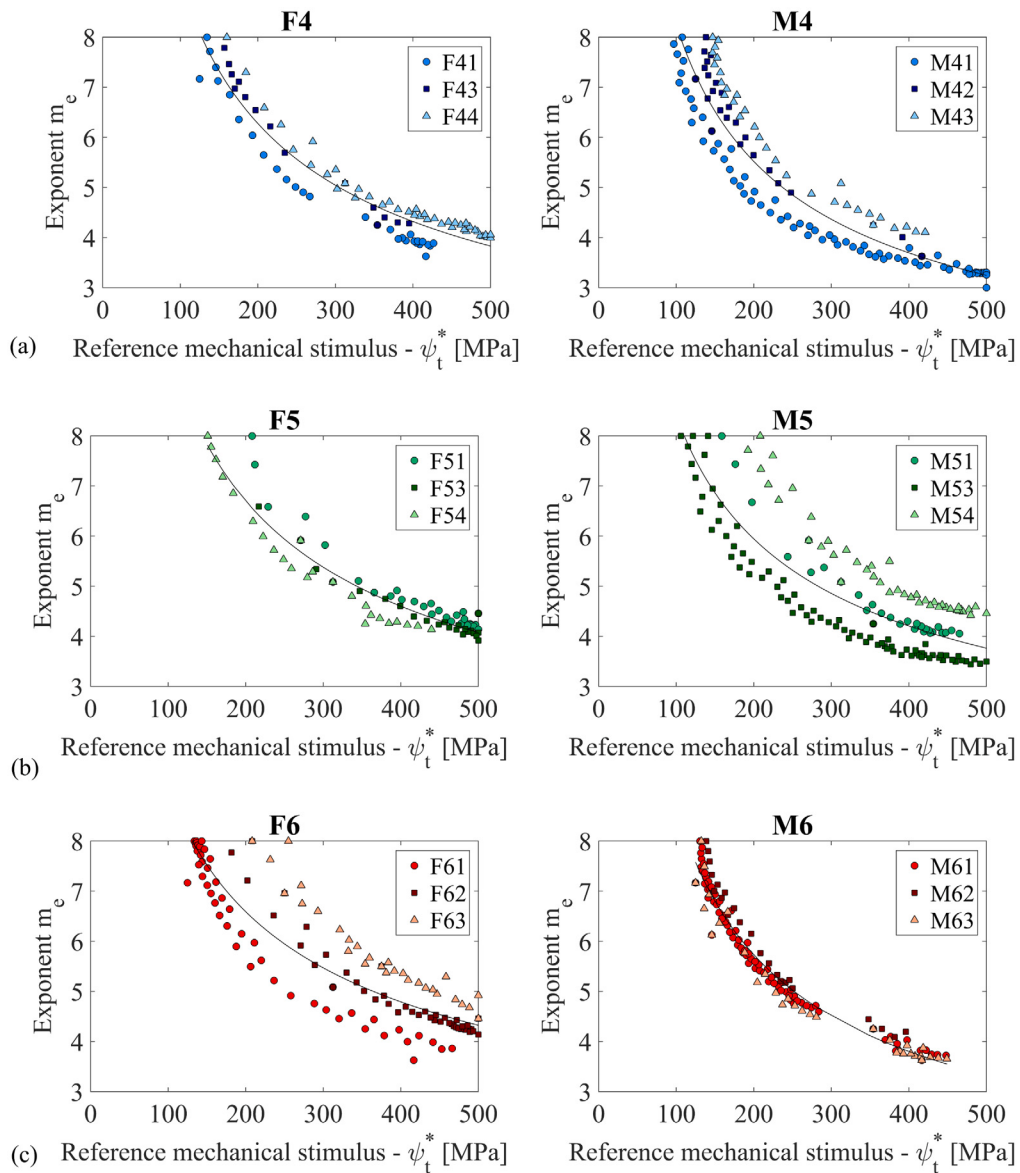


Fig. 13. Trend curve of the surrogate points that present a difference of less than 1.0% in the RDD concerning the optimum point by age range.

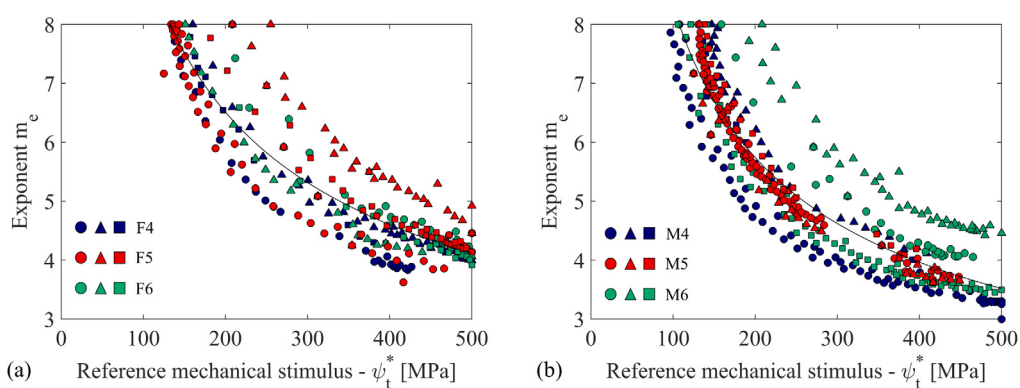


Fig. 14. Trend curve of the surrogate points that present a difference of less than 1.0% in the RDD concerning the optimum point to (a) female (F) and (b) male (M) subjects.

## CRediT authorship contribution statement

**Gabriela Wessling Oening Dicati:** Methodology, Software, Validation, Investigation, Resources, Formal analysis, Writing - Original Draft, Writing - Review & Editing, Visualization.. **José Eduardo Gubaua:** Software, Writing - Original Draft, Writing - Review & Editing, Visualization.. **Jucélio Tomás Pereira:** Conceptualization, Formal analysis, Writing - Original Draft, Writing - Review & Editing, Visualization, Supervision.

## Declaration of competing interest

The authors declare that they have no known competing financial interests or personal relationships that could have appeared to influence the work reported in this paper.

## Ethics approval

Project approved by the ethics committee of the Clinic Hospital Complex of Paraná (Presentation Certificate of Ethics Review CAAE 76467917.0.0000.0096).

## Acknowledgments

This study was financed in part by the Coordenação de Aperfeiçoamento de Pessoal de Nível Superior - Brasil (CAPES) - Finance Code 001.

## Appendix A. Supplementary data

Supplementary material related to this article can be found online at <https://doi.org/10.1016/j.euromechsol.2021.104409>.

## References

- Adachi, T., Kameo, Y., 2006. Bone modeling and remodeling. *Multiscale Mechanobiology of Bone Remodeling and Adaptation*. Springer, pp. 231–257.
- Adams, J.E., Mughal, Z., Damilakis, J., Offiah, A.C., 2012. Chapter 12: Radiology. In: Glorieux, F.H., Pettifor, J.M., Jüppner, H. (Eds.), *Pediatric Bone*, second ed. Academic Press, San Diego, pp. 277–307.
- Arun, M., Sathishkumar, N., Nitish Kumar, K., Ajai, S., Aswin, S., 2020. Development of patient specific bio-polymer incisor teeth by 3D printing process: A case study. *Mater. Today: Proc.* <http://dx.doi.org/10.1016/j.matpr.2020.04.367>.
- Ashrafi, M., Galichi, F., Mirzakouchaki, B., Doblaré, M., 2021. On the effect of antiresorptive drugs on the bone remodeling of the mandible after dental implantation: a mathematical model. *Sci. Rep.* 11 (1), 2045–2322. <http://dx.doi.org/10.1038/s41598-021-82502-y>.
- Ashrafi, M., Gubaua, J.E., Pereira, J.T., Gahlich, F., Doblaré, M., 2020. A mechano-chemo-biological model for bone remodeling with a new mechano-chemo-transduction approach. *Biochem. Model. Mechanobiol.* 19, 2499–2523. <http://dx.doi.org/10.1007/s10237-020-01353-0>.
- Avval, P., Klika, V., Bougherara, H., 2014. Predicting bone remodeling in response to total hip arthroplasty: computational study using mechanobiochemical model. *J. Biomech. Eng.* 136 (5), 051002. <http://dx.doi.org/10.1115/1.4026642>.
- Bagge, M., 1999. Remodeling of bone structures. (Ph.D. thesis). Technical University of Denmark, p. 124.
- Bahia, M.T., Hecke, M.B., Mercuri, E.G.F., Pinheiro, M.M., 2020. A bone remodeling model governed by cellular micromechanics and physiologically based pharmacokinetics. *J. Mech. Behav. Biomed. Mater.* 104, 103657. <http://dx.doi.org/10.1016/j.jmbm.2020.103657>.
- Beaupré, G.S., Orr, T.E., Carter, D.R., 1990. An approach for time dependent bone modeling and remodeling - theoretical development. *J. Orthop. Res.* 8, 651–661. <http://dx.doi.org/10.1002/jor.1100080507>.
- Belinha, J., Jorge, R.M.N., Dinis, L.M.J.S., 2013. A meshless microscale bone tissue trabecular remodelling analysis considering a new anisotropic bone tissue material law. *Comput. Methods Biomed. Eng.* 16, 1170–1184. <http://dx.doi.org/10.1080/10255842.2012.654783>.
- Bendsøe, M., Sigmund, O., 2003. *Topology Optimization - Theory, Methods, and Applications*. Springer Verlag, Germany.
- Bonewald, L.F., 2006. Mechanosensation and transduction in osteocytes. *BoneKEy Osteovis.* 3 (10), 7–15. <http://dx.doi.org/10.1138/20060233>.
- Bonewald, L.F., 2007. Osteocytes as dynamic multifunctional cells. *Ann. New York Acad. Sci.* 1116 (1), 281–290. <http://dx.doi.org/10.1196/annals.1402.018>.
- Bonewald, L.F., 2011. Osteocyte mechanosensation and transduction. *Mechanosens. Biol.* 3, 141–155. <http://dx.doi.org/10.1007/978-4-431-89757-6>.
- Boyce, B., Xing, L., 2008. Functions of RANKL/RANK/OPG in bone modeling and remodeling. *Arch. Biochem. Biophys.* 473 (2), 139–146. <http://dx.doi.org/10.1016/j.abb.2008.03.018>.
- Burgade, R., Uhl, J., Prat, G., Ruiz, C., Lorea, B., Delmas, V., Rosset, P., Le-Nail, L., 2020. 3D-modeling of sternal chondrosarcomas from angio-CT-scan: Clinical application and surgical perspectives. *Ann. 3D Print. Med.* 100003. <http://dx.doi.org/10.1016/j.stlm.2020.100003>.
- Burr, D., Allen, M., 2014. *Basic and Applied Bone Biology*. Elsevier Inc., p. 373.
- Calvo-Gallego, J.L., P., M., G.A.J., J., M.-R., 2021. A novel algorithm to resolve lack of convergence and checkerboard instability in bone adaptation simulations using non-local averaging. *Internat. J. Numer. Methods Engrg.* 37 (2), e3419. <http://dx.doi.org/10.1002/cnm.3419>.
- Cardoso, L., Fritton, S., Gailani, G., Benalla, M., Cowin, S., 2013. Advances in assessment of bone porosity, permeability and interstitial fluid flow. *J. Biomech.* 46 (2), 253–265. <http://dx.doi.org/10.1016/j.jbiomech.2012.10.025>.
- Carter, D.R., 1984. Mechanical loading histories and cortical bone remodeling. *Calcified Tissue Int.* 36, S19–S24. [http://dx.doi.org/10.1016/0021-9290\(87\)90027-3](http://dx.doi.org/10.1016/0021-9290(87)90027-3).
- Cerrolaza, M., Vanessa, D., Garzón-Alvarado, D., 2019. On mechanically driven biological stimulus for bone remodeling as a diffusive phenomenon. *Biomech. Model. Mechanobiol.* 18 (6), 1639–1663. <http://dx.doi.org/10.1007/s10237-019-01166-w>.
- Cooper, D., Thomas, C., Clement, J., Hallgrí msson, B., 2006. Three-dimensional microcomputed tomography imaging of basic multicellular unit-related resorption spaces in human cortical bone. *Anatom. Rec. A: Discov. Mole. Cell. Evolut. Biol.* 288 (7), 806–816. <http://dx.doi.org/10.1002/ar.a.20344>.
- Cowin, S. (Ed.), 2001. *Bone Mechanics Handbook*, second ed. CRC Press.
- Damon, A., Clifton, W., Valero-Moreno, F., Quinones-Hinojosa, A., 2020. Cost-effective method for 3-dimensional printing dynamic multiobject and patient-specific brain tumor models: Technical note. *World Neurosurg.* 140, 173–179. <http://dx.doi.org/10.1016/j.wneu.2020.04.184>.
- Della Corte, A., Giorgio, I., Scerrato, D., 2020. A review of recent developments in mathematical modeling of bone remodeling. *Proc. Inst. Mech. Eng. H* 234 (3), 273–281. <http://dx.doi.org/10.1177/0954411919857599>.
- Dicati, G.W.O., Gubaua, J.E., Pereira, J.T., 2020. Analysis of the uniqueness and stability of solutions to problems regarding the bone-remodeling process. *Med. Eng. Phys.* 85, 113–122. <http://dx.doi.org/10.1016/j.medengphy.2020.10.007>.
- Doblaré, M., García, J.M., 2001. Application of an anisotropic bone-remodelling model based on a damage-repair theory to the analysis of the proximal femur before and after total hip replacement. *J. Biomech.* 34 (9), 1157–1170. [http://dx.doi.org/10.1016/s0021-9290\(01\)00069-0](http://dx.doi.org/10.1016/s0021-9290(01)00069-0).
- Doblaré, M., García, J.M., 2002. Anisotropic bone remodelling model based on a continuum damage-repair theory. *J. Biomech.* 35, 1–17. [http://dx.doi.org/10.1016/S0021-9290\(01\)00178-6](http://dx.doi.org/10.1016/S0021-9290(01)00178-6).
- Doblaré, M., García, J.M., Gómez, M.J., 2004. Modelling bone tissue fracture and healing: A review. *Eng. Fract. Mech.* 71, 1809–1840. <http://dx.doi.org/10.1016/j.engfracmech.2003.08.003>.
- Forrester, A.I.J., Sóbester, A., Keane, A.J., 2007. Multi-fidelity optimization via surrogate modelling. *Proc. R. Soc. Lond. Ser. A Math. Phys. Eng. Sci.* 463, 3251–3269.
- Forrester, A.I.J., Sóbester, A., Keane, A.J., 2008. *Engineering Design Via Surrogate Modelling: A Practical Guide*, first ed. John Wiley & Sons, <http://dx.doi.org/10.1002/9780470770801>.
- Frost, H.M., 1987. Bone “mass” and the “mechanostat”: a proposal. *Anatom. Rec.* 219, 1–9. <http://dx.doi.org/10.1002/ar.1092190104>.
- Gomes, J.P.P., Costa, A.L.F., Chone, C.T., de Almeida Milani Altemani, A.M., ao Maurí cio Carrasco Altemani, J., Lima, C.S.P., 2017. Three-dimensional volumetric analysis of ghost cell odontogenic carcinoma using 3-D reconstruction software: a case report. *Oral Surg. Oral Med. Oral Pathol. Oral Radiol.* 123 (5), e170 – e175. <http://dx.doi.org/10.1016/j.joooo.2017.01.012>.
- Greenwald, A.S., Haynes, D.W., 1972. Weight-bearing areas in the human hip joint. *J. Bone Joint Surg.* 54, 157–163. <http://dx.doi.org/10.1038/2171290a0>.
- Gubaua, J.E., Dicati, G.W.O., Mercuri, E.G.F., Pereira, J.T., 2020. Simulation of bone remodeling around a femoral prosthesis using a model that accounts for biological and mechanical interactions. *Med. Eng. Phys.* 84, 126–135. <http://dx.doi.org/10.1016/j.medengphy.2020.08.004>.
- Hadjifakis, D., Androulakis, I., 2006. Bone remodeling. *Ann. New York Acad. Sci.* 1092 (1), 385–396. <http://dx.doi.org/10.1196/annals.1365.035>.
- Hall, S.J., 2007. *Basic Biomechanics*, fifth ed. McGraw-Hill, Boston, London.
- Hamblin, R., 2014. Connecting mechanics and bone cell activities in the bone remodeling process: an integrated finite element modeling. *Front. Bioeng. Biotechnol.* 2, 6. <http://dx.doi.org/10.3389/fbioe.2014.00006>.

- Hazelwood, S., Martin, R., Rashid, M., Rodrigo, J., 2001. A mechanistic model for internal bone remodeling exhibits different dynamic responses in disuse and overload. *J. Biomech.* 34 (3), 299–308. [http://dx.doi.org/10.1016/s0021-9290\(00\)00221-9](http://dx.doi.org/10.1016/s0021-9290(00)00221-9).
- Hernandez, C.J., Beaupré, G.S., Carter, D.R., 2000. A model of mechanobiologic and metabolic influences on bone adaptation. *J. Rehab. Res. Develop.* 37 (2), 235–244.
- Hinton, P., Rackard, S., Kennedy, O., 2018. In vivo osteocyte mechanotransduction: recent developments and future directions. *Curr. Osteopor. Rep.* 16 (6), 746–753. <http://dx.doi.org/10.1007/s11914-018-0485-1>.
- Huiskes, H.W.J., Weinans, H., Rietbergen, van, B., 1992. The relationship between stress shielding and bone resorption around total hip stems and the effects of flexible materials. *Clin. Orthopaed. Relat. Res.* 274, 124–134.
- Jacobs, C.R., Levenston, M.E., Beaupré, G.S., Simo, J.C., Carter, D.R., 1995. Numerical instabilities in bone remodeling simulations: The advantages of a node-based finite element approach. *J. Biomech.* 28, 449–459. [http://dx.doi.org/10.1016/0021-9290\(94\)00087-k](http://dx.doi.org/10.1016/0021-9290(94)00087-k).
- Jacobs, C.R., Simo, J.C., Beaupré, G.S., Carter, D.R., 1997. Adaptive bone remodeling incorporating simultaneous density and anisotropy considerations. *J. Biomech.* 30, 603–613. [http://dx.doi.org/10.1016/S0021-9290\(96\)00189-3](http://dx.doi.org/10.1016/S0021-9290(96)00189-3).
- Jacobs, C.R., Temiyasathit, S., Castillo, A.B., 2010. Osteocyte mechanobiology and pericellular mechanics. *Annu. Rev. Biomed. Eng.* 12 (1), 369–400. <http://dx.doi.org/10.1146/annurev-bioeng-070909-105302>.
- Klarbring, A., Torstensfelt, B., 2012. Lazy zone bone remodeling theory and its relation to topology optimization. *Ann. Solid Struct. Mech.* 4, 25–32. <http://dx.doi.org/10.1007/s12356-012-0030-3>.
- Klika, V., Pérez, M.A., García-Aznar, J.M., Maršík, F., Doblaré, M., 2014. A coupled mechano-biochemical model for bone adaptation. *J. Math. Biol.* 69, 1383–1429. <http://dx.doi.org/10.1007/s00285-013-0736-9>.
- Komarova, S.V., Smith, R.J., Dixon, S.J., Sims, S.M., Wahl, L.M., 2003. Mathematical model predicts a critical role for osteoclast autocrine regulation in the control of bone remodeling. *Bone* 33, 206–215. [http://dx.doi.org/10.1016/S8756-3282\(03\)00157-1](http://dx.doi.org/10.1016/S8756-3282(03)00157-1).
- Kowalczyk, P., 2010. Simulation of orthotropic microstructure remodelling of cancellous bone. *J. Biomech.* 43 (3), 563–569. <http://dx.doi.org/10.1016/j.jbiomech.2009.09.045>.
- Kroll, M.H., 2000. Parathyroid hormone temporal effects on bone formation and resorption. *Bull. Math. Biol.* 62 (1), 163–188. <http://dx.doi.org/10.1006/bulm.1999.0146>.
- Laz, P.J., Stowe, J.Q., Baldwin, M.A., Petrella, A.J., Rullkoetter, P.J., 2007. Incorporating uncertainty in mechanical properties for finite element-based evaluation of bone mechanics. *J. Biomech.* 40 (13), 2831–2836. <http://dx.doi.org/10.1016/j.jbiomech.2007.03.013>.
- Lemaire, V., Tobin, F.L., Greller, L.D., Cho, C.R., Suva, L.J., 2004. Modeling the interactions between osteoblast and osteoclast activities in bone remodeling. *J. Theoret. Biol.* 229, 293–309. <http://dx.doi.org/10.1016/j.jtbi.2004.03.023>.
- Martelli, S., Pivonka, P., Ebeling, P.R., 2014. Femoral shaft strains during daily activities: Implications for atypical femoral fractures. *Clin. Biomech.* 29 (8), 869–876. <http://dx.doi.org/10.1016/j.clinbiomech.2014.08.001>.
- Martin, M., Sansalone, V., Cooper, D.M.L., Forwood, M.R., Pivonka, P., 2019. Mechanobiological osteocyte feedback drives mechanostat regulation of bone in a multiscale computational model. *Biomech. Model. Mechanobiol.* 18, 1475–1496. <http://dx.doi.org/10.1007/s10237-019-01158-w>.
- Martínez-Reina, J., García-Aznar, J.M., Domínguez, J., Doblaré, M., 2009. A bone remodelling model including the directional activity of BMUs. *Biomech. Model. Mechanobiol.* 8, 111–127. <http://dx.doi.org/10.1007/s10237-008-0122-5>.
- Martínez-Reina, J., Ojeda, J., Mayo, J., 2016. On the use of bone remodelling models to estimate the density distribution of bones. Uniqueness of the solution. *PLoS One* 11, 1–17. <http://dx.doi.org/10.1371/journal.pone.0148603>.
- McNamara, L.M., Prendergast, P.J., 2007. Bone remodelling algorithms incorporating both strain and microdamage stimuli. *J. Biomech.* 40 (6), 1381–1391. <http://dx.doi.org/10.1016/j.jbiomech.2006.05.007>.
- Mercuri, E.G.F., Daniel, A.L., Hecke, M.B., Carvalho, L., 2016. Influence of different mechanical stimuli in a multi-scale mechanobiological isotropic model for bone remodelling. *Med. Eng. Phys.* 38, 904–910. <http://dx.doi.org/10.1016/j.medengphy.2016.04.018>.
- Neuert, M.A.C., Dunning, C.D., 2013. Determination of remodeling parameters for a strain-adaptive finite element model of the distal ulna. *Proc. Inst. Mech. Eng. H* 227, 994–1001. <http://dx.doi.org/10.1177/0954411913487841>.
- Opolski, A.C., Erbano, B.O., Schio, N.A., De Salles Graça, Y.L.S., Guarinello, G.G., De Oliveira, P.M.H., Leal, A.G., Foggiatto, J.A., Kubrusly, L.F., 2014. Experimental three-dimensional biomodel of complex aortic aneurysms by rapid prototyping technology. *3D Print. Addit. Manuf.* 1 (2), 88–94. <http://dx.doi.org/10.1089/3dp.2013.0009>.
- Oumghar, I.A., Barkaoui, A., Chabrand, P., 2020. Toward a mathematical modeling of diseases' impact on bone remodeling: Technical review. *Front. Bioeng. Biotechnol.* 8, 584198. <http://dx.doi.org/10.3389/fbioe.2020.584198>.
- Ozcivici, E., Luu, Y.K., Adler, B., Qin, Y.X., Rubin, J., Judex, S., Rubin, C.T., 2010. Mechanical signals as anabolic agents in bone. *Nat. Rev. Rheumatol.* 6, 50–59. <http://dx.doi.org/10.1038/nrrheum.2009.239>.
- Pastrama, M., Scheiner, S., Pivonka, P., Hellmich, C., 2018. A mathematical multiscale model of bone remodeling, accounting for pore space-specific mechanosensation. *Bone* 107, 208–211. <http://dx.doi.org/10.1016/j.bone.2017.11.009>.
- Peng, L., Bai, J., Zeng, X., Zhou, Y., 2006. Comparison of isotropic and orthotropic material property assignments on femoral finite element models under two loading conditions. *Med. Eng. Phys.* 28 (3), 227–233. <http://dx.doi.org/10.1016/j.medengphy.2005.06.003>.
- Pérez, M.A., Fornells, P., Doblaré, M., García-Aznar, J.M., 2010. Comparative analysis of bone remodelling models with respect to computerised tomography-based finite element models of bone. *Comput. Methods Biomed. Eng.* 13 (1), 71–80. <http://dx.doi.org/10.1080/10255842.2010.493728>, PMID: 19697182.
- Pérez, M.A., Moreo, P., García-Aznar, J.M., Doblaré, M., 2008. Computational simulation of dental implant osseointegration through resonance frequency analysis. *J. Biomed. Eng.* 41, 316–325. <http://dx.doi.org/10.1016/j.jbiomech.2007.09.013>.
- Pérez, M., Seral-García, B., 2013. A finite element analysis of the vibration behaviour of a cementless hip system. *Comput. Methods Biomed. Eng.* 16 (9), 1022–1031. <http://dx.doi.org/10.1080/10255842.2011.650635>.
- Pérez, M.A., Vendittoli, P.A., Lavigne, M., Nuño, N., 2014. Bone remodeling in the resurfaced femoral head: Effect of cement mantle thickness and interface characteristics. *Med. Eng. Phys.* 36 (2), 185–195. <http://dx.doi.org/10.1016/j.medengphy.2013.10.013>.
- Pivonka, P., Zimak, J., Smith, D.W., Gardiner, B.S., Dunstan, C.R., Sims, N.A., Martin, T.J., Mundy, G.R., 2008. Model structure and control of bone remodeling: A theoretical study. *Bone* 43, 249–263. <http://dx.doi.org/10.1016/j.bone.2008.03.025>.
- Reich, K.M., Gay, C.V., Frangos, J.A., 1990. Fluid shear stress as a mediator of osteoblast cyclic adenosine monophosphate production. *J. Cell. Physiol.* 143, 100–104. <http://dx.doi.org/10.1002/jcp.1041430113>.
- Rieger, R., Hamblin, R., Jennane, R., 2011. Modeling of biological doses and mechanical effects on bone transduction. *J. Theoret. Biol.* 274 (1), 36–42. <http://dx.doi.org/10.1016/j.jtbi.2011.01.003>.
- Roustant, O., Ginsbourger, D., Deville, Y., 2013. DiceKriging, DiceOptim: Two R packages for the analysis of computer experiments by Kriging-based metamodeling and optimization. *J. Stat. Softw.* 51, 1–55. <http://dx.doi.org/10.18637/jss.v051.i01>.
- Rüberg, T., García-Aznar, J.M., Doblaré, M., 2005. A bone remodelling model coupling microdamage growth and repair by 3D BMU-activity. *Biomech. Model. Mechanobiol.* 4, 147–167. <http://dx.doi.org/10.1007/s10237-005-0067-x>.
- Rungsiriyakull, C., Li, Q., Sun, G., Li, W., Swain, M.V., 2010. Surface morphology optimization for osseointegration of coated implants. *Biomaterials* 31, 7196–7204. <http://dx.doi.org/10.1016/j.biomaterials.2010.05.077>.
- Ryser, M.S., Nigam, N., Komarova, S.V., 2009. Mathematical modeling of spatio-temporal dynamics of a single bone multicellular unit. *J. Bone Miner. Res.* 24, 860–870. <http://dx.doi.org/10.1359/jbmr.081229>.
- Saeidi, M., Gubaua, J.E., Kelly, P., Kazemi, M., Besier, T., Dicati, G.W.O., Pereira, J.T., Neitzert, T., Ramezani, M., 2019. The influence of an extra-articular implant on bone remodelling of the knee joint. *Biomech. Model. Mechanobiol.* 19, 37–46. <http://dx.doi.org/10.1007/s10237-019-01193-7>.
- Schaffler, M.B., Kennedy, O.D., 2012. Osteocyte signaling in bone. *Curr. Osteoporos. Rep.* 10, 118–125. <http://dx.doi.org/10.1038/jid.2014.371>.
- Scheiner, S., Pivonka, P., Hellmich, C., 2013. Coupling systems biology with multiscale mechanics, for computer simulations of bone remodeling. *Comput. Methods Appl. Mech. Engrg.* 254, 181–196. <http://dx.doi.org/10.1016/j.cma.2012.10.015>.
- Scheiner, S., Pivonka, P., Hellmich, C., 2016. Poromicromechanics reveals that physiological bone strains induce osteocyte-stimulating lacunar pressure. *Biomech. Model. Mechanobiol.* 15, 9–28. <http://dx.doi.org/10.1007/s10237-015-0704-y>.
- Schileo, E., Taddei, F., Malandrino, A., Cristofolini, M., 2007. Subject-specific finite element models can accurately predict strain levels in long bones. *J. Biomech.* 40 (13), 2982–2989. <http://dx.doi.org/10.1016/j.jbiomech.2007.02.010>.
- Sharma, G.B., Debski, R.E., McMahon, P.J., Robertson, D.D., 2009. Adaptive glenoid bone remodeling simulation. *J. Biomech.* 42, 1460–1468. <http://dx.doi.org/10.1016/j.jbiomech.2009.04.002>.
- Simões, J.A., Vaz, M.A., Blatcher, S., Taylor, M., 2000. Influence of head constraint and muscle forces on the strain distribution within the intact femur. *Med. Eng. Phys.* 22 (7), 453–459. [http://dx.doi.org/10.1016/S1350-4533\(00\)00056-4](http://dx.doi.org/10.1016/S1350-4533(00)00056-4).
- Souza, V.H., Matsuda, R.H., Peres, A.S., Amorim, P.H.J., Moraes, T.F., Silva, J.V.L., Baffa, O., 2018. Development and characterization of the InVesalius navigator software for navigated transcranial magnetic stimulation. *J. Neurosci. Methods* 309, 109–120. <http://dx.doi.org/10.1016/j.jneumeth.2018.08.023>.
- Souza, V., Matsuda, R., Peres, A., Amorim, P., Moraes, T., Silva, J., Baffa, O., 2019. Invesalius navigator, a free and open-source software for navigated transcranial magnetic stimulation. *Brain Stimul.* 12 (2), 571. <http://dx.doi.org/10.1016/j.brs.2018.12.894>.

- Taddei, F., Cristofolini, L., Martelli, S., Gill, H.S., Viceconti, M., 2006. Subject-specific finite element models of long bones: An in vitro evaluation of the overall accuracy. *J. Biomech.* 39 (13), 2457–2467. <http://dx.doi.org/10.1016/j.jbiomech.2005.07.018>.
- Thomsen, J., Mosekilde, L., Boyce, R., Mosekilde, E., 1994. Stochastic simulation of vertebral trabecular bone remodeling. *Bone* 15 (6), 655–666. [http://dx.doi.org/10.1016/8756-3282\(94\)90314-X](http://dx.doi.org/10.1016/8756-3282(94)90314-X).
- Thomsen, J.S., Mosekilde, L., Mosekilde, E., 2020. Quantification of remodeling parameter sensitivity - assessed by a computer simulation model. *Bone* 19, 505–511. [http://dx.doi.org/10.1016/s8756-3282\(96\)00231-1](http://dx.doi.org/10.1016/s8756-3282(96)00231-1).
- Trichilo, S., Scheiner, S., Forwood, M., Cooper, D.M.L., Pivonka, P., 2019. Computational model of the dual action of PTH - application to a rat model of osteoporosis. *J. Theoret. Biol.* 473, 67–79. <http://dx.doi.org/10.1016/j.jtbi.2019.04.020>.
- Tudor-Locke, C., Craig, C.L., Thyfault, J.P., Spence, J.C., 2013. A step-defined sedentary lifestyle index: < 5000 steps/day. *Appl. Physiol. Nutr. Metabol.* 38, 100–114. <http://dx.doi.org/10.1139/apnm-2012-0235>.
- Turner, A.W.L., Gillies, R.M., Sekel, R., Morris, P., Bruce, W., Walsh, W.R., 2005. Computational bone remodelling simulations and comparisons with DEXA results. *J. Orthop. Res.* 23, 705–712. <http://dx.doi.org/10.1016/j.orthres.2005.02.002>.
- Tyrovola, J.B., Odont, X.X., 2015. The “mechanostat theory” of frost and the OPG/RANKL/RANK system. *J. Cell. Biochem.* 116 (12), 2724–2729. <http://dx.doi.org/10.1002/jcb.25265>.
- Upex, P., Jouffroy, P., Riouallon, G., 2017. Application of 3D printing for treating fractures of both columns of the acetabulum: Benefit of pre-contouring plates on the mirrored healthy pelvis. *Orthop. Traumatol.: Surg. Res.* 103 (3), 331–334. <http://dx.doi.org/10.1016/j.otrs.2016.11.021>.
- Viceconti, M., Davinelli, M., Taddei, F., Cappello, A., 2004. Automatic generation of accurate subject-specific bone finite element models to be used in clinical studies. *J. Biomech.* 37, 1597–1605. <http://dx.doi.org/10.1016/j.jbiomech.2003.12.030>.
- Weinans, H., Huiskes, R., Grootenhuis, H.J., 1992. The behavior of adaptive bone-remodeling simulation models. *J. Biomech.* 25, 1425–1441. [http://dx.doi.org/10.1016/0021-9290\(92\)90056-7](http://dx.doi.org/10.1016/0021-9290(92)90056-7).
- Whalen, R.T., Carter, D., Steele, C., 1988. Influence of physical activity on the regulation of bone density. *J. Biomech.* 21, 825–837. [http://dx.doi.org/10.1016/0021-9290\(88\)90015-2](http://dx.doi.org/10.1016/0021-9290(88)90015-2).
- You, L., Temiyasathit, S., Lee, P., Kim, C., Tummala, P., Yao, W., Kingery, W., Malone, A., Kwon, R., Jacobs, C., 2008. Osteocytes as mechanosensors in the inhibition of bone resorption due to mechanical loading. *Bone* 42 (1), 172–179. <http://dx.doi.org/10.1016/j.bone.2007.09.047>.